Post-collisional ultramafic complex in the northern North China Craton: Implications for crust-mantle interaction

Yue-Sheng Han[a], M. Santosh[a,b,c*], Nick M. W. Roberts[d], Vinod O. Samuel[e]

[a]*School of Earth Sciences and Resources, China University of Geosciences Beijing, 29 Xueyuan Road, Beijing 100083, China*

[b]*Department of Earth Sciences, University of Adelaide, SA 5005, Australia*

[c]*Yonsei Frontier Lab, Yonsei University, Seoul 03722, Republic of Korea*

[d]*Geochronology and Tracers Facility, British Geological Survey, Nottingham, UK*

[e]*Department of Earth System Sciences, Yonsei University, Seoul 03722, Republic of Korea*

Abstract

The post-collisional ultramafic intrusions within the northern margin of the North China Craton (NCC) preserve important imprints of crust-mantle interaction. Here we investigate ultramafic intrusions from the Luojianggou complex composed of pyroxenite and hornblendite associated with serpentine, with a view to gain insights into the nature of orogenic lithospheric mantle in this major continental collision zone. Zircon U-Pb data from the ultramafic suite define different age populations, with Paleoproterozoic ages (>2.2 Ga and 1.82 Ga) representing xenocrystic grains captured from the basement. The magmatic zircon grains range in age from 872 Ma to 458 Ma, and are possibly related to multiple magma emplacement associated with the Paleo-Asian Ocean closure. The youngest age of ca. 230 Ma is related to a period of post-collisional extension in the northern margin of the NCC, and this inference is further supported by apatite U-Pb ages of ~207 Ma. The mineral chemistry indicating a granulite facies condition and post-collisional setting with temperature of 700-800 ℃ and pressure of 11-13 Kbar. The pyroxenite and hornblendite show similar geochemical features and REE patterns, indicating the same magma source and formation through differentiation and accumulation. The arc-like geochemical features of the rocks with enrichment of LILE (Rb, Th and La) and LREE, but depletion of HFSE (Nb, Zr and Hf), possibly formed at the boundary of sub-continental lithospheric mantle and crust through metasomatic reaction of the overlying SCLM peridotite with the felsic melts derived from subducted materials. The arc-like features, zircon rare earth element patterns and obvious positive Pb anomaly in primitive mantle-normalized trace element spidergrams also indicate the mixing of continental materials in the magma source. The post-collisional extensional setting is

correlated to the tectonics associated with the assembly of the Mongolian arc terranes within the northern NCC during the Triassic.

Keywords: Post-collisional ultramafic intrusion; Mineral chemistry; Geochemistry; Zircon and apatite geochronology; Sub-continental lithospheric mantle

1 Introduction

Post-collisional magmatic suites provide insights into the nature of orogenic lithosphere, where the mafic rocks may record the interaction between subduction-related components and the overlying sub-continental lithospheric mantle (SCLM). The nature and composition of SCLM are influenced by different degrees of subduction-accretion and crust-mantle interaction, and hold important significance for understanding crustal evolution (Santosh, 2010). Magma sourced from the SCLM can be considered as good tracers of mantle evolution and crustal growth, and the nature of lithospheric mantle (Wilson, 1989; Miller et al., 2009; Teng et al., 2015).

The North China Craton (NCC) is one of the oldest and largest cratonic nuclei in the world, preserving crustal rocks as old as 3.8 Ga, with a complex history of crustal evolution, cratonization and stabilization (Zhao et al., 2005; Zhai and Santosh, 2011; Zhao and Zhai, 2013; Santosh et al., 2016). Following its cratonization, the NCC remained stable from the Meso-Neoproterozoic to the Early Triassic except for its northern margin, where intense deformation occurred since the Early Mesozoic, accompanied with extensive magmatism, lithospheric destruction and thinning (Davis et al., 2001; Rudnick et al., 204; Yang et al., 2008; Wu et al., 2008). The Central Asian Orogenic Belt (CAOB) defines the largest Phanerozoic accretionary orogen in the world, along which the Siberian Craton in the north and Tarim-North China Craton in the south were amalgamated (Windley et al., 2007; Xiao et al., 2003). The southern CAOB records final closure of the Paleo-Asian Ocean and the amalgamation of the North China Craton with the Mongolian arc terranes along the Solonker suture (Xiao et al., 2003; Xiao and Santosh, 2014; Safonova and Santosh, 2014). However, the nature and timing of amalgamation between the NCC and the Mongolian arc terranes is controversial, and the northern NCC has been regarded as a Paleozoic passive continental margin (Xiao et al., 2003; Xu and Chen, 1997). Some of the ultramafic-mafic complexes along the northern margin of the NCC were investigated in previous studies including the Gaositai dunite-wehrlite- pyroxenite-hornblendite complex (~244 Ma and 248 Ma, Bai et al., 1993; 224Ma and 210 Ma, Yang et al., 2017), Hongshila pyroxenite-hornblendite complex (~390 Ma, HBGMR, 1989; Bai et al., 1993), Erdaogou-

Xiahabaqin pyroxenite-hornblendite-rodingite complexes (~390 Ma, Bai et al., 1993; Ni et al., 2005), and Boluonuo hornblendite-hornblende gabbro complex (~297 Ma, Zhang et al., 2009b).

In order to understand the nature of the SCLM beneath the northern NCC and to gain more insights on the origin of the ultramafic suites in this region, we investigate the ultramafic intrusions from the Luojianggou complex through petrology, mineral chemistry, major and trace element data, zircon and apatite U-Pb geochronology, and zircon rare earth elements. Based on the results, we discuss the petrogenesis and tectonic setting of the ultramafic suite, and the nature of the crust-mantle interaction and tectonic history associated with the amalgamation of the Mongolian arc terranes with the NCC.

2 Geological background

The NCC is generally considered to be composed of the two major crustal blocks, the Eastern and Western Blocks which were finally amalgamated during Paleoproterozoic at about 1.85 Ga (Zhao et al., 2005; Zhai and Santosh, 2013; Zhao and Zhai, 2013; Santosh et al., 2015). After a long period of quiescence, the NCC was reactivated along its boundaries by the strongly influence of southward subduction of the Paleo-Asian Oceanic plate during Carboniferous to Permian, and the northern margin of the NCC is regarded as an Andean-style continental margin during late Carboniferous to early Permian (Xiao et al., 2003; Zhang et al., 2009b). The final closure of the Paleo-Asian Ocean and the accretion of Mongolian arc terranes with the northern margin of the NCC occurred during late Permian to earliest Triassic, followed by post-collisional/orogenic extension, with voluminous magmatism (Zhang et al., 2012). These tectonic processes resulted in extensive modification of the cratonic lithospheric mantle beneath the northern NCC, melt-mantle interaction and emplacement of alkaline intrusions with minor ultramafic-mafic suites during the late Paleozoic to Early Mesozoic (Zhang et al., 2009a; Hou et al., 2015). These ultramafic-mafic intrusions are mainly distributed along or adjacent to the Chicheng-Chongli-Shangyi and Damiao-Guanglingshan faults with an east-west trend (Fig. 1b). They are significant in terms of evaluating the petrological and geochemical modifications and melt-mantle interaction between the SCLM and material that has been subducted.

The Loujianggou ultramafic complex investigated in this study is located in the northern margin and adjacent to the eastern margin of the Trans-North China Orogen (TNCO) of the NCC, and it is surrounded by the Late Carboniferous-Early Permian dioritic-granitic intrusions (Fig. 1a). The complex is distributed along the Damiao-Guanglingshan Fault (Fig. 1b), and the major rock types are pyroxenite, hornblendite and serpentinite. Amphibolite, granitoids, diorite and diabase intrusions also present in the area (Fig. 2). From previous studies, HBGMR. (1989) reported the Late Carboniferous-Early

Permian plutons are distributed along the northern margin of the NCC and main consist of diorite, quartz diorite and granodiorite (Fig. 1b), and recent studies show the emplacement time of these plutons between 324 ± 6 Ma and 274 ± 6 Ma (Zhang et al., 2009c), and there is no data was reported for the amphibolite (Fig. 2).

3 Analytical methods

Polished thin sections were prepared at the School of Earth and Space Sciences, Peking University. Petrographic studies and photomicrography were performed at the Institute of Earths Sciences, China University of Geosciences, Beijing.

Electron microprobe analyses were performed on a JEOL JXA-8100 Superprobe, Electron Probe Micro Analyzer (EPMA), housed at the Earth System Sciences, Yonsei University, Seoul, South Korea. Core to rim compositions of important mineral assemblages are analyzed. Analytical conditions are used accelerating voltage of 20 kV; beam current of 20 nA; counting time of 10 s and an electron beam spot size of 5 μm. Natural and synthetic silicates and oxides supplied by JEOL and ASTIMEX standards Ltd., Canada, were used for calibration. The data were reduced using the ZAF correction procedures supplied by JEOL.

Whole rock geochemistry analyses including major, trace and rare earth elements were carried out in the Testing Center of the First Geological Institute of the China Metallurgical Geology Bureau, Sanhe City, Hebei Province. Fresh and homogeneous portions of representative ultramafic rocks were crushed and powdered to 200 mesh. Loss on ignition was obtained with sample powder (1g) heated at 980℃ for 30 min. The major elements and trace elements were analyzed by X-ray fluorescence (XRF model PW 4400) and PE300D inductive coupled plasma mass spectrometry (ICP-MS), respectively. The analytical uncertainties for major element oxides ranges from 1 to 3%. The accuracy of determination (RSD) for trace elements range from 2% to 10%. Trace and rare earth elements were analyzed with analytical uncertainties of 10% for elements with abundances <10 ppm, and approximately 5% for those >10 ppm (Gao et al., 2008).

Zircon and apatite separation for U-Pb geochronology were carried out at the Yu'neng Geological and Mineral Separation Centre, Langfang City, Hebei Province, China. The gravimetric and magnetic separation for zircon grains, and apatite grains were separated using standard mineral separation techniques (shaking table, conventional heavy-liquid, Frantz magnetic techniques). The grains were picked from each sample under a binocular microscope. They were mounted onto an epoxy resin disc and then polished to expose the internal texture. The most suitable sites for zircon U-Pb analyses were selected by checking the Cathodoluminescence (CL), transmitted and reflected light images and back-scattered electron images for apatite U-Pb analyses.

Laser Ablation Inductively Coupled Plasma Mass Spectrometry (LA-ICP-MS) zircon U-Pb geochronology was performed at the State Key Laboratory of Geological Processes and Mineral Resources (GPMR), China University of Geosciences (Wuhan) following the analytical procedures described by Liu et al. (2010a). The analyses were conducted with an Agilent 7500a ICP-MS coupled with a GeoLas 2005 laser ablation system. The spot size was 35 μm. The zircon 91500 and silicate glass NIST were used as external reference materials for the data correction and optimizing the instrument, respectively (Morel et al., 2008). The ^{29}Si mass was also measured as an internal standard to calibrate the U, Th and Pb concentrations. The raw data were processed using the ICPMSDataCal (Liu et al., 2008) program to calculate isotopic ratios and ages. Concordia diagrams and weighted mean calculations were made using ISOPLOT 4.15 software (Ludwig, 2011).

LA-ICP-MS apatite U-Pb geochronology was conducted at the British Geological Survey (Nottingham, UK) using a Nu Instruments Attom single-collector ICP-MS, coupled to a NWR 193UC excimer laser ablation system fitted with a TV2 cell. A helium flow rate of 0.7 L/min was introduced through the cell, and this was mixed at a y-piece with Ar before entering the torch. The following masses were measured, each with a dwell time of 500 μs: ^{206}Pb, ^{207}Pb, ^{208}Pb, ^{232}Th and ^{238}U. One hundred sweeps of the mass range are integrated into each datum. The value of 137.818 for $^{238}U/^{235}U$ (Hiess et al., 2012) is used for calculation of ^{235}U from the measured ^{238}U mass. Laser parameters were 40 μm static spots, ablated for 30 seconds at 10 Hz with a fluence of ~3 J/cm^2; a 5 second washout is left between each ablation. A gas background of one minute is subtracted from each run of standards and samples. A standard sample bracketing routine was used with NIST610 silicate glass (Woodhead and Hergt, 2001) for normalisation of Pb-Pb ratios, and McClure Mountain apatite (Schoene and Bowring, 2006) for U-Pb ratios. Data reduction utilised the Time Resolved Analysis function in the Nu Instruments Attolab software, and an in-house excel spreadsheet. Uncertainty propagation follows the recommendations of Horstwood et al. (2016). Additional reference materials Durango ($^{40}Ar/^{39}Ar$ age of 31.44 ± 0.18 Ma; McDowell et al., 2005) and Madagascar apatite (ca. 473; Thomson et al., 2012) were analysed alongside the unknowns as a check on accuracy. Durango, a low uranium apatite, yielded a date of 33.99 ± 0.71 Ma, and Madagascar yielded 469 ± 10 Ma.

4 Results

4.1 Sampling

Ten ultramafic rocks, including pyroxenite, hornblendite, serpentinized pyroxenite, and serpentinized dunite for this study were collected from the Luojianggou complex. The samples collected in this study come from a large open pit mining area, where several hillocks are quarried to mine ultramafic rocks to extract Ti and V (Fig. 3a). The major rock types exposed in the quarries and surrounding hillocks are medium to coarse grained pyroxenite with brownish orthopyroxene and fine grained dark grayish or black clinopyroxene. Fine grained dark gray serpentinite is also associated with veins or pockets of magnesite, suggesting that the rocks experienced hydration and carbonation (Fig. 3b). Some of the fine grained dark colored pyroxenite shows slight serpentinization (Fig. 3c). Some of the pyroxenite zones contain highly coarse grained clinopyroxene (Fig. 3d).

4.2 Petrography and mineral chemistry

The sample location, rock type and mineral assemblage are given in Table 1, and the representative photomicrographs are given in Fig. 4. The pyroxeites (LJG-1/3, LJG-1/5, LJG-1/8) and serpentinized dunite (LJG-1/9B) were also selected for EPMA analysis, and the data of representative minerals are presented in Supplementary Table 1, and representative back scattered images (BSE) of the mineral assemblages are shown in Fig. 5.

4.1.1 Pyroxenite

The representative samples LJG-1/1, LJG-1/2，LJG-1/3 and LJG-1/7 of medium to coarse grained pyroxenites display minor compositional variation, and are composed of clinopyroxene (75-85 vol.%), orthopyroxene (5-10 vol.%), and amphibole (<5 vol.%), minor opaque minerals (magnetite) and apatite and zircon as accessories (Fig. 4a). Medium to coarse grained clinopyroxene (1.2-6.8 mm) and orthopyroxene (3.1-8.9 mm) are the main matrix minerals which display cumulate texture. Minor phlogopite occurs as flaky and tabular grains in sample LJG-1/3, and the size of phlogopite flakes is in the range of 0.5-0.9 mm (Fig. 4b).

Samples LJG-1/5 and LJG-1/6 are fine to medium grained pyroxenites with clinopyroxene (75-85 vol.%), orthopyroxene (5-10 vol.%), amphibole (<5 vol.%) and magnesite (<5 vol.%) with titanite as the main accessory mineral. In thin section, the clinopyroxene is fine to medium grained (0.5-2.1 mm), and subhedral. The orthopyroxene is also fine to medium grained with a size range of 0.4 to 1.8 mm. The minerals exhibit distinct cumulate texture and little alteration (Fig. 4c).

LJG-1/8 mainly consists of clinopyroxene, magnetite and andradite (Fig. 5 a). Clinopyroxene grains are porphyroblastic have size of ~1-2mm. Magnetite present as thin veins all along the clinopyroxene grain boundaries. Anhedral grains of andradite forms along the clinopyroxene grain boundaries occasionally which size are mostly 0.25 to 0.5 mm.

The clinopyroxene composition of LJG-1/3, 1/5, 1/8 mostly vary between X_{Mg}= 0.33–0.37. Magnetite in sample LJG-1/5 is Cr rich compared to other samples (X_{Chrom}= 0.15–0.16). Magnetite in other samples are almost pure magnetite with very less Ti component (X_{Mt}= 0.98–0.99). Andradite in sample LJG-1/8 has octahedral Y site mostly made of Fe and the X site mostly have X_{Ca}=0.98–0.99.

4.1.2 Hornblendite

Sample LJG-1/4 of hornblendite is fine grained and dark gray colored in hand specimen. In thin section, the rock exhibits heterogranular texture with hornblende (~70 vol.%), clinopyroxene (~20 vol.%), orthopyroxene (<5 vol.%), and minor magnetite, apatite and zircon as accessory minerals (Fig. 4d). The hornblende (size 0.1 to 1.2 mm) is mostly greenish to brownish and subhedral and fine to medium grained, ranging in size from 0.5 to 4 mm.

4.1.3 Serpentinized pyroxenite

Sample LJG-1-9A is serpentinized pyroxenite and is fine grained and dark gray colored, showing massive texture in hand specimen. In thin section, the rock is mainly composed of clinopyroxene (~60 vol.%), serpentine (~25 vol.%) and orthopyroxene (<5 vol.%), with magnetite, talc and actinolite as accessory minerals (Fig. 4e). Most of the pyroxenes were altered to serpentine, talc and actinolite, and the relict grains are mainly clinopyroxene with the size in range of 0.4-1.3 mm. Some clinopyroxenes have a serrated boundary and show serpentinization. The actinolite grains show tabular relic shape and slight radial pattern.

4.1.4 Serpentinized dunite

The serpentinized dunite (LJG-1-9B) is brownish and fine grained, showing a massive texture in hand specimen. In thin section, the sample shows serpentinization, and is composed of olivine (10-15 vol.%), and serpentine (85-90 vol.%), with magnetite as an accessory mineral (Fig. 4f, Fig. 5b). The relict olivine shows fine grained (0.1-0.5 mm) subhedral granular texture and the grains are sporadically present within the serpentine matrix. Thin veins of magnetite are present along with the serpentine matrix. The serpentinite is distributed along the grain boundaries and display irregular network to form a mesh texture.

Serpentine in sample LJG-1/9B is a composition between lizardite and antigorite (X_{Mg}= 0.51-0.53). Olivine in this sample has X_{Mg}= 0.90–0.91. Mineral composition plots show that andradite falls between grossular and almandine composition (Fig. 6a),and olivine is forsteritic (Fig. 6b), and clinopyroxene has mostly diopsidic composition (Fig. 6c).

4.3 Geochemistry

Whole rock geochemical analyses including major, trace and rare earth elements were performed on eight samples from the Luojianggou complex. These samples include pyroxenites and hornblendite and the result are listed in Table 2.

The pyroxenites (sample LJG-1/1, LJG-1/2, LJG-1/3, LJG-1/7 and LJG-1/8) show low concentrations of SiO_2 (33.76-42.96 wt%) and moderate contents of MgO (9.64-13.23) as well as relatively moderate magnesium number in the range of 44.91-57.72, typical of derivation from evolved mafic magma. They have relatively high TiO_2 (0.82-1.33 wt%), Al_2O_3 (2.98-3.48), FeO (6.59-9.05 wt%), Fe_2O_3 (11.86-15.23 wt%) and TFe_2O_3 (19.18-25.14 wt%), and CaO (18.79-20.75 wt%). In contrast, the pyroxenite samples LJG-1/5 and LJG-1/6 show higher concentrations of SiO_2 (53.59-53.64) and MgO (17.30-16.77) and magnesium number (88.17-89.20). They have relatively low TiO_2 (0.17-0.15 wt.%), Al_2O_3 (1.16-1.07), FeO (2.73-2.67 wt%), Fe_2O_3 (1.56-1.05 wt%) and TFe_2O_3 (4.60-4.02 wt%), and high CaO (23.16-23.35 wt%). All pyroxenite samples show low K_2O (0.01-0.74 wt%) and Na_2O (0.14-0.24 wt%) contents, and the concentration of LOI in the range of 0.20-0.37 wt% except LJG-1/1 is 5.18 wt% (Table 2). The composition of hornblendite (sample LJG-1/4) is broadly similar to that of the low Mg# pyroxenite, and shows low SiO_2 (36.67 wt%) content, and moderate FeO (8.02 wt%), high Fe_2O_3 (14.06 wt%), TFe_2O_3 (22.96 wt%) and MgO (11.22 wt%) with magnesium number is 49.18. It is also shows low concentrations of TiO_2 (1.11 wt%), moderate Al_2O_3 (3.67 wt%) and high CaO (19.94 wt%), with low K_2O (0.19 wt%), Na_2O (0.27 wt%) and LOI (0.68 wt%) (Table 2). The LOI (<6 wt.%) and lack of mobile elements (e.g. K, Na) in these samples, suggest possible slight alteration only, which is further confirmed by their negligible Ce anomalies (0.90-0.97) (Table 2).

The studied rocks have similar features of trace elements, except for samples LJG-1/5 and LJG-1/6 with higher Cr (1972-1687 ppm), lower Ti (963-879 ppm) and V (43.68-44.57 ppm), respectively. The remaining samples show higher Ti (up to 7610 ppm) and V (up to 679 ppm), lower Cr (12.75-57.00 ppm) (Table 2). The pyroxenites and hornblendite show similar patterns on the chondrite-normalized REE patterns and primitive mantle-normalized spider diagrams (Fig. 7). All samples show convex patterns with peaks at Pr-Sm, and without obvious Eu anomalies (0.92-1.19) (Fig. 7a,c), suggesting the clinopyroxene and hornblende megacrysts precipitated from high pressures condition and originated as cumulates, and balanced with light-REE enriched basaltic melts (Irving, 1974; Irving and Frey, 1984). The rocks display moderate LREE enrichment with $(La/Yb)_N$ ratios in the range of 4.59-13.47 (Fig. 7a,c). In the primitive mantle-normalized trace element spidergram (Fig. 7b,d), they are characterized by enrichment of LILE (Rb, Th, La) but depletion of HFSE (Nb, Zr, Hf). Samples LJG-1/2 and LJG-1/7 show negative K anomalies, and LJG-1/3, LJG-1/5, LJG-1/6 and LJG-1/7 display negative P anomalies, corresponding to their relatively low K_2O (0.01-0.02 wt.%) and P_2O_5 (0.002-0.04

wt.%) contents, respectively (Fig. 7d) (Table 2).

The selected major oxides from rock types show some systematic variation against their MgO content (Fig. 8), suggesting fractional crystallization. In general, the Al_2O_3 and TFe_2O_3 values show negative correlation with the increase of MgO (Fig. 8a,b). The distribution of CaO values are constant (Fig. 8c), whereas the total Na_2O and K_2O values are scattered (Fig. 8d). There are two samples (LJG-1/5 and LJG-1/6) show low TFe_2O_3 and Al_2O_3 contents, and combined with the high MgO content, implying the samples lost Fe-oxides during fraction evolution, it is also supported by the characteristics in the thin section which lack of magnetite (Fig. 4c). The concordant relationship between CaO and MgO may be related to the generation of clinopyroxene and hornblende, both of which are important hosts of calcium. The scattered correlation of total Na_2O and K_2O values versus MgO (Fig. 8d), is consistent with minor plagioclase in these samples, which is also further supported by their slight Eu anomalies (Fig. 7a,c and Table 2). The distinct correlations of the major oxides observed from Hongshila and Erdaogou-Xiahabaqin ultramafic complex with this study (Fig. 8), combined with their different age populations, implying the formation of these intrusions were different magmatic pulses.

4.4 Zircon U-Pb geochronology

Three representative samples were analyzed for zircon geochronology from the Luojianggou complex, including two pyroxenites (LJG-1/1 and LJG-1/7) and one serpentinized pyroxenite (LJG-1/9A). Representative CL images, and concordia diagrams of age data are given in Fig. 9 and Fig. 10, and the data are listed in Supplementary Table 2.

4.4.1 Pyroxenite

Two representative samples of pyroxenite were analyzed for zircon U-Pb dating. Zircon grains from pyroxenite sample LJG-1/1 are grayish or dark brownish, and subhedral to euhedral. Some grains show irregular shape, whereas others display elliptical shape. Their length ranges 35 μm to 180 μm with aspect ratios of 2:1-1:1. Under CL images, some grains are structureless and homogeneous with rare grains showing faint zoning, and others carrying distinct oscillatory zoning, along with few xenocrystic zircons (Fig. 9a). Thirty-one spots were analysed on 31 zircon grains from this sample among which twelve spots are excluded due to low concordance. The youngest two concordant spots yield a weighted mean $^{206}Pb/^{238}U$ age of 230.7 ± 2.9 Ma (MSWD = 0.15) with Th/U ratios are 0.02 and 0.07 (Fig. 10a,b). Seven spots yield $^{206}Pb/^{238}U$ ages from 699 Ma to 458 Ma, with Th/U ratios in the range of 0.32-2.06, and three concordant spots yield a weighted mean $^{206}Pb/^{238}U$ age of 824 ± 19 Ma (MSWD = 1.4) with Th/U ratios range from 0.63 to 0.80 (Fig. 10a). Two spots yield older $^{207}Pb/^{206}Pb$ age of 1828 ± 78 Ma and 1818 ± 62 Ma with

Th/U ratios of 1.13 and 0.11. Four spots defining the oldest ages yield $^{207}Pb/^{206}Pb$ ages in the range of 2550-2261 Ma, with Th/U ranging from 0.57 to 0.73 (Supplementary Table 2).

Zircon grains from pyroxenite sample LJG-1/7 are colorless or brownish, subhedral to euhedral and translucent. Some grains are sub-rounded and others show elliptical shape with length in the range of 40-70 μm, and aspect ratios of 1.5:1-1:1. In the CL images, some of the zircon grains are homogeneous, and some grains show core-rim textures with dark colored oscillatory zoning and light colored rims, suggesting a metamorphic overprint (Fig. 9b). Fifteen spots were analyzed on 15 zircon grains from this sample, and excluding eight spots that have low concordance, the remaining spots can be divided into three groups. The first group includes four spots, two of which yield a weighted mean $^{206}Pb/^{238}U$ age of 808.5 ± 9.6 Ma (MSWD = 0.83, n = 2), with Th/U ratios in the range of 0.61-0.71 (Fig. 10c,d). The second group includes two concordant spots with a weighted mean $^{207}Pb/^{206}Pb$ age of 1806 ± 37 Ma (MSWD = 0.81), and Th/U of 0.02 and 1.64. The last concordant spot yielded a $^{207}Pb/^{206}Pb$ age of 2572 ± 58 Ma, with Th/U ratio value of 0.34 (Supplementary Table 2).

4.4.2 Serpentinized pyroxenite

Zircon grains from serpentinized pyroxenite sample LJG-1/9A are dark brownish and subhedral. Some grains are elliptical in shape and one grain is elongate; their length is in the range of 50-170 μm with aspect ratios of 4:1-1:1. Under CL images, few grains are homogeneous and show chaotic texture. Oscillatory and faint banded zoning are also present, representing magmatic crystallization (Fig. 9c). In total, nineteen spots were analyzed on 19 zircon grains from this sample, among which six spots with low concordance are excluded. The youngest two spots yield $^{206}Pb/^{238}U$ ages of 213 ± 8.59 Ma and 230 ± 5.17 Ma with Th/U values of 0.91 and 0.80 (Fig. 10e,f). There are two spots that yield $^{206}Pb/^{238}U$ ages of 549 Ma and 717 Ma, and two concordant spots show a weighted mean $^{206}Pb/^{238}U$ age of 809 ± 11 Ma (MSWD = 0.016, n = 2) with Th/U values of 0.31 and 1.96. The older age data can be divided into two groups; the first group includes two spots with weighted mean $^{207}Pb/^{206}Pb$ age of 1818 ± 69 Ma (MSWD = 0.041) and values of 1.36 and 0.91 (Fig. 10e). The second group yields a weighted mean $^{207}Pb/^{206}Pb$ age of 2433 ± 64 Ma (MSWD = 0.25, n = 2), with Th/U values of 0.35 and 0.79 (Supplementary Table 2).

4.5 Apatite U-Pb geochronology

Apatite is a ubiquitous accessory mineral occurring in almost all major rock types, and is commonly employed for thermochronology studies by U/Th-He and fission track dating (Farley and Stockli, 2002). Apatite is also an ideal mineral for dating the emplacement age through the application of U-Pb system for rapidly cooled plutonic rocks (Cherniak, 2005), especially when other minerals suitable for dating are not readily available. Since zircon grains are inadequate in the ultramafic rocks of the present study, and their age data are complex, we separated apatite from six representative samples for U-Pb dating, among which samples LJG-1/1 and LJG-1/3 were excluded due to high abundance of common lead.

A total of 25 spots were analyzed on apatite from pyroxenite sample LJG-1/5, and excluding three spots with large uncertainties, the remaining spots when plotted on a Tera-Wasserburg diagram yield a lower intercept U-Pb age of 200.7 ± 7.3 Ma (MSWD = 1.5, n = 22) (Fig. 11a). Their U contents are in the range of 1.0-14 ppm, and Th in the range of 1.6-80 ppm, with Th/U ratios of 1.7-17.1 (Supplementary Table 3). Twenty-five spots were analyzed in apatite from both pyroxenite samples LJG-1/7 and LJG-1/8 among which one spot from LJG-1/7 and two from LJG-1/8 were excluded because of their large uncertainties. When plotted on Tera-Wasserburg diagrams, these yield lower intercept ages of 204.6 ± 8.2 Ma (MSWD = 1.7, n = 24) and 208.3 ± 9.5 Ma (MSWD = 2.6, n = 23) (Fig. 11b,c), respectively. Their U contents range from 0.7 ppm to 10 ppm and 9.2 ppm to 26 ppm, Th contents of 7-37 ppm and 48-126 ppm, with Th/U ratios in the range of 2.9-22.2 and 3.3-6.0, respectively (Supplementary Table 3).

Twenty-four spots were analyzed from serpentinized pyroxenite LJG-1/9A, among which six spots were excluded because of large uncertainties. The remaining spots using a Tera-Wasserburg plot yield a lower intercept age of 219 ± 24 Ma (MSWD = 1.5, n = 18) (Fig. 11d), with Th and U contents in the range of 12-49 ppm and 6.9-15 ppm, and Th/U ratios of 1.6-3.8 (Supplementary Table 3).

4.6 Zircon rare earth elements

The chondrite-normalized REE patterns of the zircon trace element data show LREE depletion and HREE enrichment (Fig. 12) (Supplementary Table 4). Some zircon grains from pyroxenite (LJG-1/1, LJG-1/7), and serpentinized pyroxenite (LJG-1/9A) show relatively flat patterns of REE with slight positive Ce anomalies (Ce/Ce* = 1.18-12.87) and negative or positive Eu anomalies (Eu/Eu* = 0.09-1.29). The REE patterns of these zircon grains are similar to those of zircon crystallization from hydrous melts (Hoskin, 2005), The other grains show distinct positive Ce anomalies (Ce/Ce* = 14.19-204.76) and negative Eu anomalies (Eu/Eu* = 0.04-0.72), typical of magmatic zircon (Hoskin and Schaltegger, 2003).

5 Discussion

5.1 Implications of zircon and apatite U-Pb age

Phanerozoic ultramafic-mafic intrusions are widely distributed along the northern margin of the NCC (Tian et al., 2007; Zhao et al., 2007) and the timing of their emplacement is important for studying the tectonic evolution of this collisional margin. Our study is the first comprehensive attempt to obtain coupled zircon and apatite U-Pb ages from the Luojianggou ultramafic complex and to investigate the implications of post-collision extension.

In our study, zircon grains from studied samples (LJG-1/1, LJG-1/7 and LJG-1/9A) show concordant $^{207}Pb/^{206}Pb$ ages of 2432 ± 69 Ma, 2261 ± 69 Ma and 2571 ± 58 Ma and a weighted mean age of 2433 ± 64 Ma (Fig. 10a,c,e). The corresponding zircon grains display growth zoning or homogeneous texture (Fig. 9), suggesting that the ages represent the timing of emplacement or metamorphism. Two groups of zircon grains from the samples yielded weighted mean $^{207}Pb/^{206}Pb$ age of 1806 ± 37 Ma and 1818 ± 69 Ma, and one group yielded $^{207}Pb/^{206}Pb$ age of 1828 ± 78 Ma and 1818 ± 62 Ma, respectively (Fig. 10a,c,e). The zircon grains are typically structureless and homogeneous, representing metamorphic growth. The ~2.4 Ga and ~1.8 Ga ages correlate well with the extensive early Paleoproterozoic magmatism and late Paleoproterozoic metamorphism in the NCC basement (Zhai and Santosh, 2011). In this study, the Neoarchean-Paleoproterozoic zircons in the samples can be considered to inject into the sunduction zone which from the reworking of ancient sources or older detrital zircons from subducting sediments.

One of the major zircon populations in our study show Neoproterozoic weighted mean $^{206}Pb/^{238}U$ ages of 824 ± 19Ma, 808.5 ± 9.6Ma and 809 ± 11 Ma (Fig. 10a,c,e), and these grains possess typical oscillatory zoning (Fig. 9), suggesting that they are magmatic origin. Zircon growth in the range of 699-458 Ma is also indicated (Fig. 10b,d,f) (Supplementary Table 2). From previous studies, the opening time of Paleo-Asian Ocean is considered to have started at 900 Ma, and the early accretion and collision events during 700-600 Ma are mainly related to the collision between micro-continents and the Siberian continent (Li, 2006; Dobretsov et al., 1995; Yang et al., 2017). Thus, the Neoproterozoic age of ca. 810 Ma can be considered to represent the initial subduction stage of the Paleo-Asian Ocean, and the Paleozoic age populations are related to magmatic pulses during the different stage of subduction. Some of the zircon grains in the samples show inherited core with narrow metamorphic rims, and these grains may be captured during the magma ascend along the continental channel.

The youngest zircon age populations in our samples yield a weighted mean $^{206}Pb/^{238}U$ age of 230.7 ± 2.9 Ma, and concordant $^{206}Pb/^{238}U$ spot ages of 230 ± 5 Ma and 213 ± 8 Ma, respectively (Fig. 10a,e), and they are much younger than surrounding dioritic-granitic rocks. The limited number of dates in these youngest populations precludes a precise estimate of the crystallization age based on zircon. The apatite in our samples show U and Th contents in the range of 0.7-26 ppm and 1.6-126 ppm (Supplementary Table 3), suggesting that their U-Pb ages are reliable, when considering the initial Pb isotopic composition (Amelin and Zaitsev, 2001). Four samples (LJG-1/5, LJG-1/7, LJG-1/8 and LJG-1/9A) yield overlapping Tera-Wasserburg lower intercept ages of 200.7 ± 7.3 Ma, 204.6 ± 8.2 Ma, 208.3 ± 9.5 Ma and 219 ± 24 Ma, respectively (Fig. 11). Collectively, these data indicate that the intrusive complex had intruded by 230 Ma, and had cooled below ca. 500 °C by 205 Ma. The final closure of Paleo-Asian Ocean and the amalgamation of the Mongolian arc terranes with the NCC are considered to have taken place in the late Permian to earliest Triassic (~250 Ma) (Xiao et al., 2003; Li, 2006), followed by post-collisional/post-orogenic extension, with extensive magmatism and continental growth (Zhang et al., 2009b). In a previous study, some zircon grains from the ultramafic rocks of the Gaositai complex yielded $^{206}Pb/^{238}U$ ages of 224 Ma and 210 Ma (Yang et al., 2017). Tian et al. (2007) also reported zircon SHRIMP U-Pb ages of Late Triassic mafic-ultramafic rocks from Xiaozhangjiakou complex which were emplaced at 220 Ma. Zhang et al, (2009a) proposed that the emplacement age of the Triassic mafic-ultramafic rocks on the north NCC corresponds to the post-collisional/post orogenic extension.

5.2 Petrogenetic implications

The Luojianggou ultramafic intrusion is characterized by clinopyroxene and hornblende-rich assemblages, with minor orthopyroxene and the absence of plagioclase assemblages, and the rocks show typical cumulate texture (Fig. 4), and they also display different differentiation curves in the variation diagrams (Fig. 8). They also show similar chondrite-normalized REE patterns (Fig. 7a,c) and primitive mantle-normalized trace element patterns (Fig. 7b,d), implying that they formed from the same magma source.

Ultramafic-mafic magmatic complexes emplaced in continental crust are generally considered as the products of fractional crystallization of mafic magmas, with pyroxenite and hornblendite representing the plutonic cumulate phase of anhydrous and hydrous basaltic melts, respectively. In either case, the mafic melts originate from partial melting of ultramafic lithologies such as peridotite, pyroxenite and hornblendite. Several scenarios have been proposed for the petrogenesis of cumulate pyroxenite, including primary magma partially melted from lithospheric mantle or asthenospheric mantle (Irving, 1980; Suen and Frey, 1987), formation through the reaction between mantle peridotite and silica-enriched melts released by subducted slab (Kelemen, 1995; Kelemen et al., 1998), and residual melt after re-partial melting of previous mantle-derived magma (Frey and Prinz, 1978). It is known that the input of silica transforms the original magma into basaltic composition, and in this study, all the rocks exhibit a tholeiitic trend on the AFM diagram (Fig. 13a) (Beard, 1986), and two of the samples are extremely magnesium-rich (Fig. 13b). All samples also fall in the region of the arc-related mafic cumulate field (Fig. 13a). These features suggest the influence of convergent margin processes and components derived from subducted slabs.

Generally, there are two mechanisms to incorporate crustal materials into mafic melts in continental regions: crustal contamination, and source mixing (Zheng, 2012). Crustal contamination involves the addition of crustal compositions to the mantle-derived magmas when they ascend through the continental crust, and the source mixing refers to mixture of crustal and mantle-derived materials into magma sources before partial melting. In this study, the ultramafic intrusions from Luojianggou complex exhibit medium to high contents of MgO (9.64-17.30 wt.%), with magnesium number in the range of 44.91-89.20, but low SiO_2 contents of 33.76-53.64 wt.% (Table 2), implying that they were derived from ultramafic-mafic mantle rocks. However, they also show enrichment in LILEs (Rb, Th and La) and LREEs, but depletion of HFSEs (Nb, Zr and Hf) in the chondrite-normalized REE patterns and primitive mantle-normalized trace element spidergrams (Fig. 7). In addition, all samples show typical positive Pb anomalies, indicating different levels of contamination with upper continental crustal compositions or input from subducted sediments into the basaltic melts. The plots of Th/Yb-Nb/Yb (Fig. 14a) can also confirm this inference, where they fall in the region of active continental margins with slight oceanic arc system features and enrichment trend, suggesting that the magma was derived from enriched sources. The rocks also show an affinity with continental crust (both Middle Crust – MC, and Lower Crust - LC) (Fig. 14a), and in the Th/Ta-La/Yb diagram (Fig. 14b), with Lower Crust (LC) and Upper Crust (UC), implying contamination from the continental crust during magmatic crystallization, which also is supported by the xenocrystic zircon grains in the samples. These features suggest significant contamination of continental crust during ascent of the mantle-derived magmas.

As outlined before, the arc-like trace element signature argues against partial melting of the asthenospheric mantle. All the plots show negligible affinity with the MORB field (Fig. 14a), and this inference is also confirmed by Nb/U and Ce/Pb ratios, which are in the range of 1.32-13.96 and 0.17-2.59, respectively (Table 2), they are markedly different from the MORB and OIB (Nb/U ≈ 47 and Ce/Pb ≈ 25; Hofmann, 1988). As discussed above, we exclude the influence of the asthenospheric mantle as the source, and in this active continental setting, we infer that the sub-continental lithospheric mantle source with significant contamination of continental crustal materials.

It is generally accepted that the extensive dehydration was present of downgoing subducted oceanic slabs, and results in the removal of water-soluble elements such as LILE and LREE (Becker et al., 2000; John et al., 2004), and island arc magmatism is correlated to extensive release of metasomatic fluids into the overlying mantle wedge (Tatsumi and Eggins, 1995). Hermann et al. (2006) and Spandler et al. (2007) proposed that hydrous felsic melts are most effective agents for transfer of large amounts of trace elements from the slab to the mantle wedge than aqueous fluids. Therefore, it is possible that the mantle source for the ultramafic rocks of Luojianggou complex were formed through metasomatism by the overlying SCLM with the felsic melts derived from the subducted slab and overlying sediments. In the U-Yb and U/Yb-Y discrimination diagrams (Fig. 15a,b), the zircon grains are characterized by obvious continental crust features, suggesting the involvement of continental crustal components in the magma source. However, partial melting of the refractory SCLM is restricted due to low water content, as well as low Al_2O_3 and CaO but high MgO content. The 'enriched' or 'continental crust-like' signature of the trace elements in the studied samples can be considered to have resulted from partial melting of the enriched SCLM-crust domains (Rudnick, 1995; Dai et al., 2012). However, the Mg# (44.91-57.72) of most samples are not equilibrium with the mantle, we envisage the possible origin of the parental magma at the mantle-crust boundary, with the crustal signature from subducted sediments (Teng et al., 2015; and references therein). The reaction of mantle peridotite component with crustal materials makes the magma homogeneous and more enriched in silica. At the same time, the input of silica converts the original magma into a basaltic composition.

In this study, the Mongolian arc terranes subducted beneath the northern margin of the North China Craton including the ancient SCLM during the Triassic, resulted in slab-mantle interaction in the continental subduction channel, with the SCLM-wedge peridotite refertilized by fluid alteration and melt metasomatism (Zheng, 2012). The limited volume of aqueous fluids released by the subducted cold continental crust, can only partially alter the SCLM domains in the orogenic lithospheric mantle, and cannot lead to extensive arc magmatism. In contrast, the exhumation of the deeply subducted continental crust would result in partial melting induced by aqueous fluids released by subduction and breakdown of hydrous minerals, and the exsolution of structural hydroxyl and molecular water from nominally anhydrous minerals (Zheng et al., 2003; Xia et al., 2008; Chen et al., 2011). Therefore, the continental crust-derived felsic melts with arc-like features would be transferred to the mantle source of post-collisional mafic magma. The subsequent melt-peridotite reaction would generate pyroxenite and hornblendite, with the residual olivine grains. This inference is supported by the negative Eu anomalies (0.04-0.88) (Supplementary Table 4) from most of the zircon grains which crystallizated from melt-peridotite interaction. Liu et al. (2010b) reported magmatic zircon grains showing typical negative Eu anomalies (average Eu/Eu* = 0.42) in pyroxenite veins which were generate through melt-metasomatised mantle peridotite. The minor fluids also caused slight serpentinization, through the reaction: orthopyroxene + fluid = serpentine + talc or clinopyroxene + fluid = serpentine + Ca^{2+} +H_2O + $SiO_{2(aq)}$ (Frost and Beard, 2007).

Post-collisional intrusion also occurs in an ultrahigh-pressure setting, in order to evaluate the petrogenesis, a pseudosection has been constructed using bulk chemistry data of sample LJG-1/8 (Table 2). This sample consists of clinopyroxene, andradite and ulvospinel (magnetite). PERPLE_X 6.7.9 version available at http:/www.perplex.ethz.ch (Connolly, 1990, 2005, 2009) and thermodynamic data file of Holland and Powell (2003) is used for calculations. The following mineral solid solution models were used for phase diagram calculation: clinopyroxene (Cpx; Holland and Powell, 1996); garnet (Gt; Holland and Powell, 1998); Olivine (Ol; Holland and Powell, 1998); calcite (Cc; Anovitz, Essene, 1987).

The caculated pseudosection represents different stages of evolution of sample LJG-1/8 (Fig. 16), which has clinopyroxene as major mineral with andradite and ulvospinel along the clinopyroxene boundaries. The maximum X_{Mg}=0.3 of clinopyroxene in this sample is stable in the field with assemblage Ol-Cpx-Usp. This indicate that the clinopyroxene has crystallized during a high temperature pressure condition more than 800°C and 13kbar respectively. This could be related to the formation of Ol-Cpx cumulates due to the melting of peridotite. Following this the presence of andradite and magnetite forms on the grain boundaries of clinopyroxene. This stage is represented by X_{Mg}=0.34 of clinopyroxene and X_{Ca}=0.99 of andradite. During this stage sample is exhumed at a fast rate but with temperature reducing at a low rate. This could be represented as due to the infiltration of fluid during the post collisional extensional stage. Following this the sample took again a normal cooling and exhumation phase. Thus, the peak metamorphic conditions from the pseudosection modelling shows a temperature of 700–800°C and pressure of 11–13kbar during post-collisional settings, where the andradite and ulvospinel formed along the grain boundaries of clinopyroxene. These features also indicate a typical granulite facies condition. In normal geothermal conditions 10 Kbar is ~30 Km, and we can estimate the formation depth of this ultramafic intrusions are ca. 35 km, and metamorphic andradite and magnetite formed at ~25 to 30 Km.

5.3 Tectonic implications

The North China Craton experienced a complex history of extensive magmatism, metamorphism and tectonic processes during the late Archaean and Paleoproterozoic associated with the craton building. Previous studies have proposed westward subduction of the Eastern Block beneath the Western Block and final amalgamation along the Trans-North China Orogen during late Paleoproterozoic at ca. 1.85 Ga (Santosh, 2010; Santosh et al., 2015; Tang and

Santosh., 2018). In this study, the oldest zircon age population (>2.2 Ga) can be considered to be captured from the basement, and the age population of ~1.82 Ga correlates with the metamorphism associated with the collisional event. Li. (2006) proposed the opening time of the Paleo-Asian Ocean at 900 Ma, and early accretion-collision events during 700-600 Ma, with the final closure during late Permian (~250 Ma). Yang et al. (2017) reported Neoproterozoic (836-712 Ma) and middle Paleozoic (401-386 Ma) zircon $^{206}Pb/^{238}U$ ages from the Gaositai ultramafic-mafic complex in the northern margin of the NCC, and correlated its genesis with the initial subduction of the Paleo-Asian Ocean and magma emplacement events. The age populations of 872-458 Ma can therefore be correlated with the prolonged subduction of the Paleo-Asian Ocean. The late Permian Guanglingshan granite pluton formed in the post-collision setting, and was strongly deformed by shearing due to distribution along the Damiao-Guanglingshan shear zone (Zhang et al., 2009b). Hou et al. (2015) also reported post-collisional Triassic (~218 Ma) alkaline ultramafic-syenite complex at the northern margin of the NCC, and it is similar to the Middle Triassic Jianping post-orogenic granitoids (Zhang et al., 2009b). As discussed above, the zircon U-Pb age (~230 Ma) and apatite U-Pb age (~207 Ma) are considered to mark the post-collisional period of accretion of the Mongolian micro-continents along the northern margin of the NCC.

Based on the above, we propose a two-stage model to explain the formation of the Luojianggou ultramafic complex as follows: (1) The reaction between hydrous felsic melts derived from the subducted continental crust and overlying SCLM-wedge peridotite generated the enriched SCLM-crust domains (Fig. 17a). These domains characterized by low magnesium and enriched in pyroxene and hornblende. These features suggest a fertile origin and enrichment of LREE, LILE (Rb, Th and La) and Pb, depletion of HFSE (Nb, Zr and Hf); (2) Partial melting of these enriched SCLM-crust domains, with magma ascend along the continental channel, contamination of the upper continental crust, and then fractional crystallization and crystal accumulation generated the post-collision ultramafic rocks (Fig. 17b). Some Paleozoic and even much older zircon grains were captured from the continental crust during the ultramafic-mafic magma ascent; and (3) The final stage is crystallization of the Luojianggou ultramafic complex.

6 Conclusion

(1) The Luojianggou ultramafic complex was emplaced during the late Triassic as indicated by the U-Pb ages of zircon (~230 Ma) and apatite (~205 Ma). The magmatism was associated with the post-collisional extension in the northern margin of the NCC. The range of zircon ages from Neoproterozoic to Early Paleozoic correspond to the subduction-accretion-collision history of the Paleo-Asian Ocean. The Paleoproterozoic age (>2.2 Ga) and ca. 1.82 Ga from

the zircon grains indicate captured grains from the basement of the NCC.

(2) The geochemical data shows arc-like features with enrichment of Pb, LILE (Rb, Th and La) and LREE, but depletion of HFSE (Nb, Zr and Hf) and HREE. Combined with texture and mineral assemblage, we infer that the ultramafic rocks formed by fractional crystallization and crystal accumulation from tholeiitic mafic magma.

(3) The enriched SCLM domains from the Triassic collisional were formed by the incorporation of the continental components in the subduction channel. The metasomatic reaction of the overlying SCLM-peridotite with hydrous felsic melts derived from the subducted continental components generated the parent magmas which were emplaced at the boundary of enriched sub-continental lithospheric mantle and crust.

(4) The mineral chemistry features indicating that the Luojianggou ultramafic intrusions formed in a granulite facies condition, with metamorphic temperature of 700-800 ℃ and pressure of 11-13 Kbar.

Acknowledgements

We are grateful to Prof. Michael Roden and two anonymous referees for constructive comments which helped in improving our paper. This study was supported by Fundamental Research Funds for the Central Universities (Grant

No. 2652018153) to Yuesheng Han, and the 2017R1A6A1A07015374 (Multidisciplinary study for assessment of large earthquake potentials in the Korean Peninsula) through the National Research Foundation of Korea (NRF) funded by the Ministry of Science and ICT, Korea to V. O. S, and Foreign Expert position of M. Santosh at the China University of Geosciences, Beijing, China. We thank Shanshan Li, Chengxue Yang, Haidong Liu and Jingyi Wang for their valuable guidance and help during the field work and sample collection.

References

Amelin, Y., Zaitsev, A. N., 2002. Precise geochronology of phoscorites and carbonatites: the critical role of u-series disequilibrium in age interpretations. Geochimica et Cosmochimica Acta 66(13), 0-2419.

Anovitz, L., Essene, E.J., 1987. Phase equilibria in the system CaCO3-MgCO3-FeCO3. Journal of Petrology 28, 389-414.

Bai, W.J., Zhou, M.F., Hu, X.F., Cai, Y.C., Zheng, X.H., 1993. Mafic–ultramafic Magmatism and Tectonic Evolution of the North China Craton. Seismology Press, Beijing. 294 pp. (in Chinese with English abstract).

Beard, J.S., 1986. Characteristic mineralogy of arc-related cumulate gabbros: implications for the tectonic setting of gabbroic plutons and for andesite genesis. Geology 14 (10), 848–851.

Becker, H., Jochum, K.P., Carlson, R.W., 2000. Trace element fractionation during dehydration of eclogites from high-pressure terranes and the implications for element fluxes in subduction zones. Chemical Geology 163, 65–99.

Cherniak, D.J., 2005. Uranium and manganese diffusion in apatite. Chemical Geology 219, 297–308.

Chen, R.-X., Zheng, Y.-F., Gong, B., 2011. Mineral hydrogen isotopes and water contents in ultrahigh-pressure metabasite and metagranite: constraints on fluid flow during continental subduction-zone metamorphism. Chemical Geology 281, 103–124.

Condie, K.C., 1997. Sources of Proterozoic mafic dyke swarms: constraints from Th/Ta and La/Yb ratios. Precambrian Research 81, 3–14.

Connolly, J.A.D., 1990. Multivariable phase-diagrams - an algorithm based on generalized thermodynamics. American Journal of Science, 290, 666-718.

Connolly, J.A.D., 2005. Computation of phase equilibria by linear programming: A tool for geodynamic modeling and its application to subduction zone decarbonation. Earth and Planetary Science Letters, 236, 524-541.

Connolly, J.A.D., 2009. The geodynamic equation of state: what and how. Geochemistry, Geophysics, Geosystems, 10, Q10014.

Davies, J.F., Grant, R.W.E., Whitehead, R.E.S., 1979. Immobile trace elements and Archean volcanic stratigraphy in the Timmins mining area, Ontario. Canadian Journal of Earth Sciences 16 (2), 305–311.

Davis, G.A., Zheng, Y.D., Wang, C., Darby, B.J., Zhang, C.H., Gehrels, G.E., 2001. Mesozoic tectonic evolution of the Yanshan fold and thrust belt, with emphasis on Hebei and Liaoning Provinces, Northern China. In: Hendrix, M.S., Davis, G.A. (Eds.), Paleozoic and Mesozoic Tectonic Evolution of Central Asia: From Continental Assembly to Intracontinental Deformation. Geological Society of America Memoir, vol. 194, 171–197.

Dai, L.Q., Zhao, Z.F., Zheng, Y.F., & Zhang, J., 2012. The nature of orogenic lithospheric mantle: geochemical constraints from postcollisional mafic-ultramafic rocks in the dabie orogen. Chemical Geology 334(1), 99-121.

Dobretsov, N.L., Berzin, N.A., Buslov, M.M., 1995. Opening and tectonic evolution of the Paleo-Asian Ocean. International Geology Review 37 (4), 335–360.

Farley, K.A., Stockli, D.F., 2002. (U–Th)/He dating of phosphates: apatites, monazite, and xenotime. In: Kohn, M.J., Rakovan, J., Hughes, L.M. (Eds.), Phosphates: geochemical, geobiological, and materials importance: Reviews in Mineralogy & Geochemistry, 48, 559–577.

Frey, F.A., Prinz, M., 1978. Ultramafic inclusions from San Carlos, Arizona: petrologic and geochemical data bearing on their petrogenesis. Earth and Planetary Science Letters 38, 129–176.

Frost, B.R., Beard, J.S., 2007. On silica activity and serpentinization. Journal of Petrology 48, 1351–1368.

Gao, S., Rudnick, R.L., Xu, W.L., Yuan, H.L., Liu, Y.S., Walker, R.J., Puchtel, I.S., Liu, X., Huang, H., Wang, X.R., Yang, J., 2008. Recycling deep cratonic lithosphere and generation of intraplate magmatism in the North China Craton. Earth and Planetary Science Letters 270, 41–53.

Grimes, C.B., John, B.E., Kelemen, P.B., Mazdab, F.K., Wooden, J.L., Cheadle, M.J., Hanghøj, K., Schwartz, J.J., 2007. Trace element chemistry of zircons from oceanic crust: a method for distinguishing detrital zircon provenance. Geology 35, 643–646.

HBGMR, 1989. Regional Geology of Hebei Province, Beijing Municipality and Tianjin Municipality. Geol. Pub. House, Beijing. 741 pp. (in Chinese with English abstract).

Hermann, J., Spandler, C., Hack, A., Korsakov, A.V., 2006. Aqueous fluids and hydrous melts in high-pressure and ultra-high pressure rocks: implications for element transfer in subduction zones. Lithos 92, 399–417.

Hiess, J., Condon, D.J., McLean, N. and Noble, S.R., 2012. 238U/235U systematics in terrestrial uranium-bearing minerals. Science, 335(6076), 1610-1614.

Hofmann, A.W., 1988. Chemical differentiation of the earth: the relationship between mantle, continental crust and oceanic crust. Earth and Planetary Science Letters 90, 297–314.

Hoskin, P.W., Schaltegger, U., 2003. The composition of zircon and igneous and metamorphic petrogenesis. Reviews in Mineralogy and Geochemistry 53 (1), 27–62.

Hoskin, P.W.O., 2005. Trace-element composition of hydrothermal zircon and the alteration of Hadean zircon from the Jack Hills. Australia. Geochimica et Cosmochimica Acta 69 (3), 637–648.

Hou, T., Zhang, Z., Keiding, J. K., & Veksler, I. V., 2015. Petrogenesis of the Ultrapotassic Fanshan intrusion in the North China Craton: implications for lithospheric mantle metasomatism and the origin of apatite ores. Journal of Petrology 56(5), 251-256.

Horstwood, M.S.A., Košler, J., Gehrels, G., Jackson, S.E., McLean, N.M., Paton, C., Pearson, N.J., Sircombe, K., Sylvester, P., Vermeesch, P. and Bowring, J.F., 2016. Community‐derived standards for LA‐ICP‐MS U‐(Th‐) Pb geochronology–Uncertainty propagation, age interpretation and data reporting. Geostandards and Geoanalytical Research 40(3), 311-332.

Holland, T., Powell, R., 1996. Thermodynamics of order-disorder in minerals. 2.

Symmetric formalism applied to solid solutions. American Mineralogist **81**, 1425-37.

Holland, T., Powell, R., 2003. Activity-composition relations for phase in petrological calculations: an asymmetric multicomponent formulation. Contributions to Mineralogy and Petrology 145, 492-501.

Holland, T.J.B., Powell, R., 1998. An internally consistent thermodynamic data set for phases of petrological interest. Journal of Metamorphic Geology **16**, 309-343.

Irvine, T.N., Baragar, W.R.A., 1971. A guide to the chemical classification of the common volcanic rocks. Canadian Journal of Earth Sciences 8, 523–548.

Irving, A.J., 1974. Geochemical and high pressure experimental studies of garnet pyroxenite and pyroxene granulite xenoliths from the Delegate basaltic pipes, Australia. Journal of Petrology 15, 1–40

Irving, A.J., 1980. Petrology and geochemistry of composite ultramafic xenoliths in alkali basalts and implications for magmatic processes within the mantle. American Journal of Science 280, 389–426.

Irving, A.J., Frey, F.A., 1984. Trace element abundances in megacrysts and their host basalts: constraints on partition coefficients and megacryst genesis. Geochimica et Cosmochimica Acta 48, 1201–1221.

John, T., Scherer, E.E., Haase, K., Schenk, V., 2004. Trace element fractionation during fluid-induced eclogitization in a subducting slab: trace element and Lu–Hf–Sm–Nd isotope systematics. Earth and Planetary Science Letters 227, 441–456.

Kelemen, P.B., 1995. Genesis of high Mg# andesites and the continental crust. Contributions of Mineralogy and Petrology 120, 1–19.

Kelemen, P.B., Hart, S.R., Bernstein, S., 1998. Silica enrichment in the continental upper mantle via melt/rock reaction. Earth and Planetary Science Letters 164, 387–406.

Kuno, H., 1968. Origin of andesite and its bearing on the island arc structure. Bulletin Volcanologique 32, 141–176.

Li, J.Y., 2006. Permian geodynamic setting of Northeast China and adjacent regions: closure of the Paleo-Asian Ocean and subduction of the Paleo-Pacific Plate. Journal of Asian Earth Sciences 26 (3), 207–224.

Liu, Y., Zong, K., Kelemen, P.B., Gao, S., 2008. Geochemistry and magmatic history of eclogites and ultramafic rocks from the Chinese continental scientific drill hole: subduction and ultrahigh-pressure metamorphism of lower crustal cumulates. Chemical Geology 247:133–153.

Liu, Y.S., Hu, Z.C., Zong, K.Q., Gao, C.G., Gao, S., Xu, J., Chen, H.H., 2010a. Reappraisement and refinement of zircon U-Pb isotope and trace element analyses by LA-ICP-MS. Chinese Science Bulletin 55:1535–1546.

Liu, Y.S., Gao, S., Hu, Z.C., Gao, C.G., ZKQ, Wang, D.B., 2010b. Continental and oceanic crust recycling-induced melt–peridotite interactions in the Trans-North China Orogen: U-Pb dating, Hf isotopes and trace elements in zircons from mantle xenoliths. Journal of Petrology 51, 537–571.

Ludwig, K.R., 2011. Isoplot v. 4.15: a geochronological toolkit for Microsoft Excel. Berkeley Geochronology Center Special Publication 4, 75 pp.

McDonough, W.F., Sun, S.S., 1995. The composition of the Earth. Chemical Geology 120 (3–4), 223–253.

McDowell, F.W., McIntosh, W.C. and Farley, K.A., 2005. A precise 40Ar–39Ar reference age for the Durango apatite (U–Th)/He and fission-track dating standard. Chemical Geology 214(3-4), 249-263.

Miller, R.B., Paterson, S.R., Matzel, J.P., 2009. Plutonism at different crustal levels: insights from the 5–40 km (paleo depth) North Cascades crustal section, Washington. In: Miller, R.B., Snoke, A.W. (Eds.), Crustal Cross Sections from the Western North American Cordillera and Elsewhere: Implications for Tectonic and Petrologic Processes. Geological Society of America Special Paper 456, 125–149.

Morel, M.L.A., Nebel, O., Nebel-Jacobsen, Y.J., Miller, J.S., Vroon, P.Z., 2008. Hafnium isotope characterization of the GJ-1 zircon reference material by solution and laserablation MC-ICPMS. Chemical geology 255 (1), 231–235.

Ni, Z.Y., Zhai, M.G., Zhao, T.P., Zhou, L., 2005. Petrology of rodingites and their petrogenetical significance. Advance in Earth Sciences 20, 407–413. (in Chinese with English abstract).

Parlak, O., Höck, V., Delaloye, M., 2002. The supra-subduction zone Pozanti–Karsanti ophiolite, southern Turkey: evidence for high-pressure crystal fractionation of ultramafic cumulates. Lithos 65, 205–224.

Pearce, J.A., 2008. Geochemical fingerprinting of oceanic basalts with applications to ophiolite classification and the search for Archean oceanic crust. Lithos 100 (1–4), 14–48.

Rudnick, R.L., 1995. Making continental crust. Nature 378, 571–578.

Rudnick, R.L., Gao, S., Ling, W.L., Liu, Y.S., McDonough, W., 2004. Petrology and geochemistry of spinel peridoite xenoliths from Hannuoba and Qixia, North China Craton. Lithos 77, 609–637.

Santosh, M., 2010. Assembling North China Craton within the Columbia supercontinent: the role of double-sided subduction. Precambrian

Research 178 (1), 149–167.

Santosh, M., Yang, Q. Y., Teng, X., Tang, L., 2015. Paleoproterozoic crustal growth in the north china craton: evidence from the lüliang complex. Precambrian Research 263, 197-231.

Santosh, M., Teng, X.M., He, X.F., Tang, L., Yang, Q.Y., 2016. Discovery of Neoarchean suprasubduction zone ophiolite suite from Yishui Complex in the North China Craton. Gondwana Research 38, 1–27.

Safonova, I.Yu., Santosh, M., 2014. Accretionary complexes in the Asia-Pacific region: tracing archives of ocean plate stratigraphy and tracking mantle plumes. Gondwana Research 25, 126–158.

Schoene, B. and Bowring, S.A., 2006. U–Pb systematics of the McClure Mountain syenite: thermochronological constraints on the age of the 40 Ar/39 Ar standard MMhb. Contributions to Mineralogy and Petrology 151(5), p.615.

Spandler, C., Mavrogenes, J., Hermann, J., 2007. Experimental constraints on element mobility from subducted sediments using high-P synthetic fluid/melt inclusions. Chemical Geology 239, 228–249.

Sun, S.S., Mc Donough, W.F., 1989. Chemical and isotopic systematics of oceanic basalts: implications for mantle composition and processes. In: Saunders, A.D., Norry, M.J. (Eds.), Magmatism in Ocean Basins. Geological Society of London Special Publication, 313–345.

Suen, C.J., Frey, F.A., 1987. Origins of the mafic and ultramafic rocks in the Ronda peridotite. Earth and Planetary Science Letters 85, 183–202.

Tang, L., Santosh, M., 2018. Neoarchean-Paleoproterozoic terrane assembly and Wilson cycle in the North China Craton: an overview from the central augment of the TransNorth China Orogen. Earth-Science Reviews 182, 1–27.

Tatsumi, Y., Eggins, S., 1995. Subduction Zone Magmatism. Blackwell Science, Oxford. 211 pp.

Teng, X., Q Y, Y., Santosh, M., 2015, Devonian magmatism associated with arc-continent collision in the northern North China Craton: Evidence from the Longwangmiao ultramafic intrusion in the Damiao area. Journal of Asian Earth Sciences 113, 626–643.

Thomson, S.N., Gehrels, G.E., Ruiz, J. and Buchwaldt, R., 2012. Routine low-damage apatite U‐Pb dating using laser ablation–multicollector–ICPMS. Geochemistry, Geophysics, Geosystems 13(2).

Tian, W., Chen, B., Liu, C.Q., Zhang, H.F., 2007. Zircon U–Pb age and Hf isotopic composition of the Xiaozhangjiakou ultramafic pluton in northern Hebei: Acta Petrologica Sinica, v. 23, p. 583–590. (in Chinese with English abstract).

Wilson, B.M., 1989. Igneous Petrogenesis a Global Tectonic Approach. Chapman & Hall, London, p. 466.

Windley, B.F., Alexeiev, D., Xiao, W., Kröner, A., Badarch, G., 2007. Tectonic models for accretion of the Central Asian Orogenic Belt. Journal of the Geological Society 164, 31–47.

Woodhead, J.D. and Hergt, J.M., 2001. Strontium, neodymium and lead isotope analyses of NIST glass certified reference materials: SRM 610, 612, 614. Geostandards Newsletter 25(2-3), 261-266.

Wu, F.Y., Xu, Y.G., Gao, S., Zheng, J.P., 2008. Lithospheric thinning and destruction of the North China Craton. Acta Petrologica Sinica 24, 1145–1174. (in Chinese with English abstract).

Xiao, W., Windley, B.F., Hao, J., Zhai, M.G., 2003. Accretion leading to collision and the Permian Solonker suture, Inner Mongolia, China: termination of the central Asian orogenic belt. Tectonics 22, 1069.

Xiao, W.J., Santosh, M., 2014. The western Central Asian Orogenic Belt: a window to accretionary orogenesis and continental growth. Gondwana Research 25, 1429–1444.

Xia, Q.-X., Zheng, Y.-F., Zhou, L.-G., 2008. Dehydration and melting during continental collision: constraints from element and isotope geochemistry of low-T/UHP granitic gneiss in the Dabie orogen. Chemical Geology 247, 36–65.

Xu, B., Chen, B., 1997. Framework and evolution of the middle Paleozoicorogenic belt between Siberian and north China plates in northern InnerMongolia. Science in China Series D Earth Sciences 40, 463–479.

Yang, J.H., Wu, F.Y., Wilde, S.A., Belousova, E., Griffin, W.L., 2008. Mesozoic decratonization of the North China Block. Geology 36, 467–470.

Yang, F., Santosh, M., Tsunogae, T., Tang, L., Teng, X.M., 2017. Multiple magmatism in an evolving suprasubduction zone mantle wedge: The case of the composite maficultramafic complex of Gaositai, North China Craton. Lithos 284–285, 525–544.

Zhai, M.G., Santosh, M., 2011. The early Precambrian odyssey of the North China Craton: a synoptic overview. Gondwana Research 20 (1), 6–25.

Zhai, M., Santosh, M., 2013. Metallogeny of the north china craton: link with secular changes in the evolving earth. Gondwana Research, 24(1), 275-297.

Zhao, G. C. Sun, M., Wilde, S. A., and Li, S. Z., 2005. Late Archean to Paleoproterozoic evolution of the North China Craton: key issues revisited. Precambrian Research. 136(2), 177-202.

Zhao, G. C., and Zhai, M. G., 2013. Lithotectonic elements of precambrian basement in the North China Craton: review and tectonic implications. Gondwana Research. 23(4), 1207-1240.

Zhao, Z. F., Dai, L. Q., Zheng, Y. F., 2013. Postcollisional mafic igneous rocks record crust-mantle interaction during continental deep subduction. Scientific Reports 3.

Zhao, G., Wilde, S. A., Li, S., Sun, M., Grant, M. L., Li, X., 2007. U-Pb zircon age constraints on the dongwanzi ultramafic-mafic body, North China, confirm it is not an archean ophiolite. Earth and Planetary Science Letters 255(1-2), 0-93.

Zhang, S. H., Zhao, Y., Liu, X. C., Liu, D. Y., Chen, F., Xie, L. W., et al., 2009a. Late paleozoic to early mesozoic mafic–ultramafic complexes from the northern north china block: constraints on the composition and evolution of the lithospheric mantle. Lithos 110(1-4), 229-246.

Zhang, S.H., Zhao, Y., Song, B., Hu, J.M., Liu, S.W., Yang, Y.H., Chen, F.K., Liu, X.M., Liu, J., 2009b. Contrasting Late Carboniferous and Late Permian–Middle Triassic intrusive suites from the northern margin of the North China craton: geochronology, petrogenesis and tectonic implications. Geological Society of America Bulletin 121,181–200.

Zhang, S.H., Zhao, Y., Kröner, A., Liu, X.M., Xie, L.W., Chen, F.K., 2009c. Early

Permian plutons from the northern North China Block: constraints on continental arc evolution and convergent margin magmatism related to the Central Asian Orogenic Belt. International Journal of Earth Sciences 98, 1441–1467.

Zhang, S. H., Zhao, Y., Ye, H., Hou, K. J., Li, C. F., 2012. Early Mesozoic alkaline complexes in the northern North China Craton: Implications for cratonic lithospheric destruction. Lithos 155, 1–15.

Zheng, Y.-F., 2012. Metamorphic chemical geodynamics in continental subduction zones. Chemical Geology 328, 5–48.

Zheng, Y.-F., Fu, B., Gong, B., Li, L., 2003. Stable isotope geochemistry of ultrahigh pressure metamorphic rocks from the Dabie–Sulu orogen in China: implications for geodynamics and fluid regime. Earth-Science Reviews 62, 105–161.

Figure captions

Fig. 1 Schematic map showing (a) regional geological and tectonic framework and (b) distribution of Late Paleozoic-Early Mesozoic ultramafic-mafic complexes and study area in the northern NCC (modified after Zhang et al., 2009a). Complex names: XZJK, Xiaozhangjiakou; LY, Liuying; BLN, Boluonuo; HSL, Hongshila; EX, Erdaogou-Xiahabaqin; GST, Gaositai; LJG, Luojianggou. Fault names: CCSF, Chicheng-Chongli-Shangyi Fault; FLF, Fengning-Longhua Fault; DGF, Damiao-Guanglingshan Fault; PGF, Pingquan-Gubeikou Fault.

Fig. 2 Geological sketch map of Luojianggou ultramafic complex with sampling location.

Fig. 3 Representative photographs of the ultramafic rocks in this study. (a) A large open cast mining area with pyroxenite. (b) White colored magnesite surrounded by fine grained dark gray serpentinite and dark grayish pyroxenite. (c) Fine grained dark colored pyroxenite with slight serpentinization. (d) Coarse grained clinopyroxene rich rock.

Fig. 4 Representative photomicrographs (in cross-polarized light) of the samples from Luojianggou complex. (a, b, c) Pyroxenite samples of LJG-1/2, LJG-1/3 and LJG-1/5, respectively. (d) Hornblendite sample of LJG-1/4. (e) Serpentinized pyroxenite sample of LJG-1/9A. (f) Serpentinized dunite samples of LJG-1/9B. Mineral abbreviations: Cpx, clinopyroxene; Opx, orthopyroxene; Amp, amphibole; Mgt, magnetite; Phl, phlogopite; Hbl, hornblende; Ap, apatite; Act, actinolite; Srp, serpentine; Tc, Talc; Ol, olivine.

Fig. 5 Representative back scattered electron images (BSE) of thin sections from the samples selected for Electron Microprobe Analyses showing the mineral assemblage of studied rocks. Abbreviations of minerals: Mt, magnetite; Cpx, clinopyroxene; Adr, andradite; Srp, serpentine; Ol, olivine.

Fig. 6 Compositional diagrams showing the chemistry of representative minerals in pyroxenite and serpentinized dunite. (a) shows andradite composition of garnet formed in pyroxenites. (b) representative forsterite composition of olivine grains in the serpentinized dunite sample and (c) shows that clinopyroxene in pyroxenite and serpentinized dunite samples have diopside composition.

Fig. 7 Chondrite-normalized rare earth element (REE) patterns (a, c) and primitive mantle-normalized trace element variation diagrams (b, d) for analyzed samples from Luojianggou complex. Normalized values: chondrite (McDonough and Sun, 1995), primitive mantle (Sun and McDonough, 1989).

Fig. 8 Co-variation diagrams showing MgO versus Al_2O_3 (a), TFe_2O_3 (b), CaO (c), Na_2O + K_2O (d) and comparison with the previous data. Complex names: LJG, Luojianggou; HSL: Hongshila; EX, Erdaogou-Xiahabaqin.

Fig. 9 Representative Cathodoluminescence (CL) images of zircon grains from pyroxenite (samples LJG-1/1 and LJG-1/7) and serpentinized pyroxenite (sample LJG-1/9A). The analytical spots for U-Pb and age with yellow circles are shown.

Fig. 10 Zircon U-Pb Concordia plots (a, c, e) and age data histograms with probability curves (b, d, f) for samples LJG-1/1, LJG-1/7 and LJG-1/9A.

Fig. 11 Tera-Wasserburg concordia diagrams for apatite dating from samples LJG-1/5, LJG-1/7, LJG-1/8 and LJG-1/9A.

Fig. 12 Chondrite-normalized zircon REE patterns (Sun and Mc Donough, 1989) from the Luojianggou ultramafic samples.

Fig. 13 (a) Ternary plot of TFeO - Na_2O + K_2O – MgO from studied samples. The black curve is from Kuno (1968) and the red one is from Irvine and Baragar (1971), and the fields of cumulate and non-cumulate rocks are from Parlak et al., 2002. (b) Ternary plot of TiO_2*100-Y + Zr-Cr (Davies et al., 1979).

Fig. 14 Representative trace and rare earth elements based ratio diagrams illustrating the petrogenetic characteristics of the Luojianggou samples. (a) Th/Yb vs. Nb/Yb plot (Pearce, 2008) and (b) Th/Ta vs. La/Yb plot, and the positions of mantle and crustal components are from Condie, 1997. Abbreviations: DM, depleted mantle; PM, primitive mantle; EM1 and EM2, enriched mantle sources; LC, lower continental crust; UC, upper continental crust; CC, continental crust.

Fig. 15 (a) U vs. Yb, and (b) U/Yb vs. Y plots from the result of zircon REE data, the fields for continental or MORB source are from Grimes et al., 2007.

Fig. 16 Phase diagram of pyroxenite from Luojianggou ultramafic intrusions, using sample LJG-1/8 (phase diagram constructed following Connolly, 1990, 2005, 2009; Holland and Powell, 1998).

Fig. 17 Schematic plate tectonic model explaining the evolution of the Luojianggou ultramafic intrusion in the northern margin of the NCC (modified after Zhao et al., 2013). (a) Reaction of the overlying SCLM peridotite with hydrous felsic melts derived from the subducted continental components, generating the enriched SCLM domains during Triassic continental collision. (b) Partial melting of the fertile and enriched SCLM domains, followed by fractional crystallization and crystal accumulation to form the post-collisional ultramafic rocks.

Table captions

Table 1 Summary of locations, GPS co-ordinates, rock types and mineral assemblages of the samples analyzed in this study.

Table 2 Whole-rock Geochemistry data of the Luojianggou ultramafic intrusion in this study.

Supplementary Tables

Supplementary Table 1 The result of Electron microprobe analyses of representative minerals from the analyzed samples.

Supplementary Table 2 LA-ICP-MS U-Pb data for zircon grains from pyroxenites (LJG-1/1 and LJG-1/7) and serpentinized pyroxenite (LJG-1/9A) of Luojianggou ultramafic complex.

Supplementary Table 3 U-Th-Pb analytical results of apatite grains from studied samples.

Supplementary Table 4 Zircon rare earth element concentration of analyzed samples from Luojianggou complex.

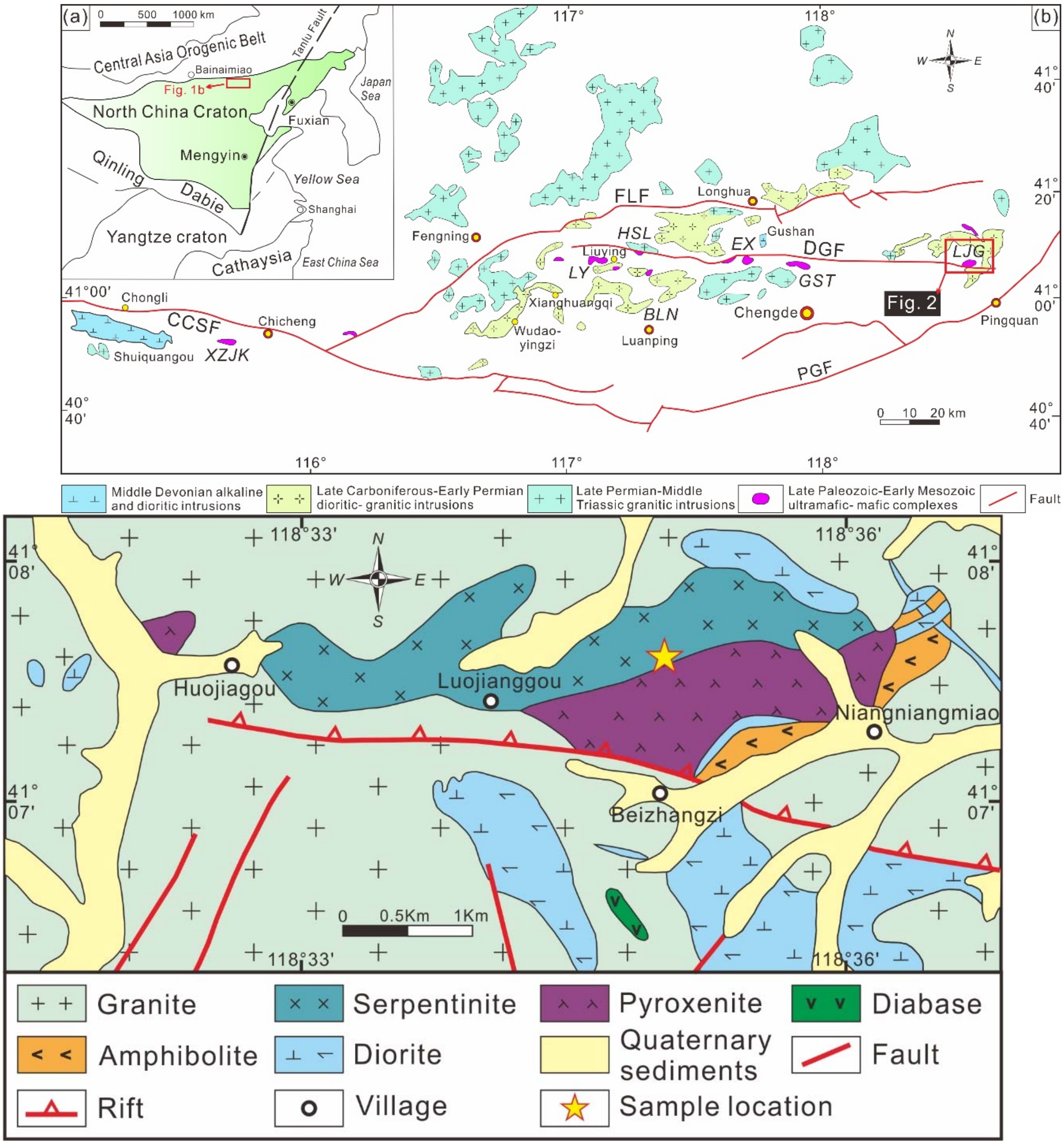

1094 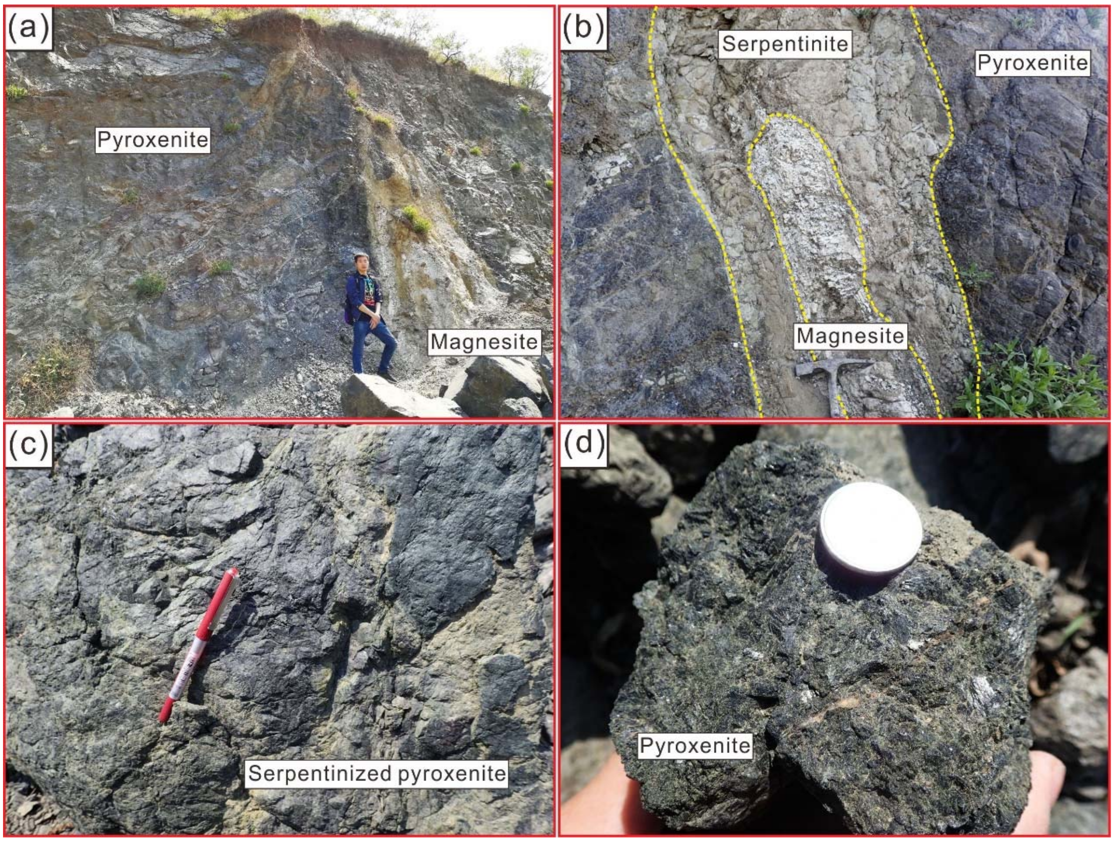
(a)
Pyroxenite
Magnesite
(b)
Serpentinite
Pyroxenite
Magnesite
(c)
Serpentinized pyroxenite
(d)
Pyroxenite

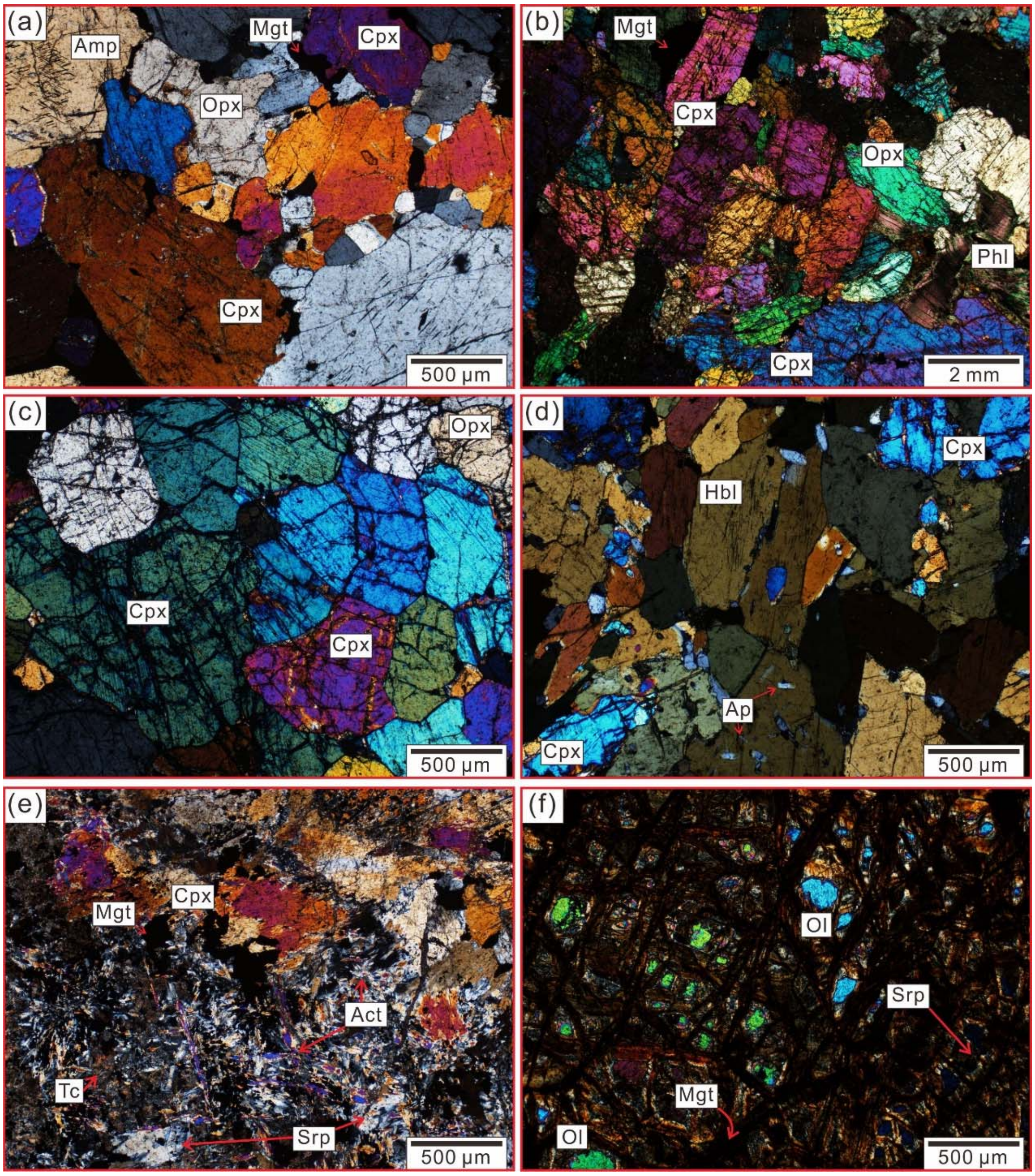
(a)
Amp
Mgt
Cpx
Opx
Cpx
500 μm
(b)
Mgt
Cpx
Opx
Phl
Cpx
2 mm
(c)
Opx
Cpx
Cpx
500 μm
(d)
Cpx
Hbl
Ap
Cpx
500 μm
(e)
Mgt
Cpx
Act
Tc
Srp
500 μm
(f)
Ol
Srp
Mgt
Ol
500 μm

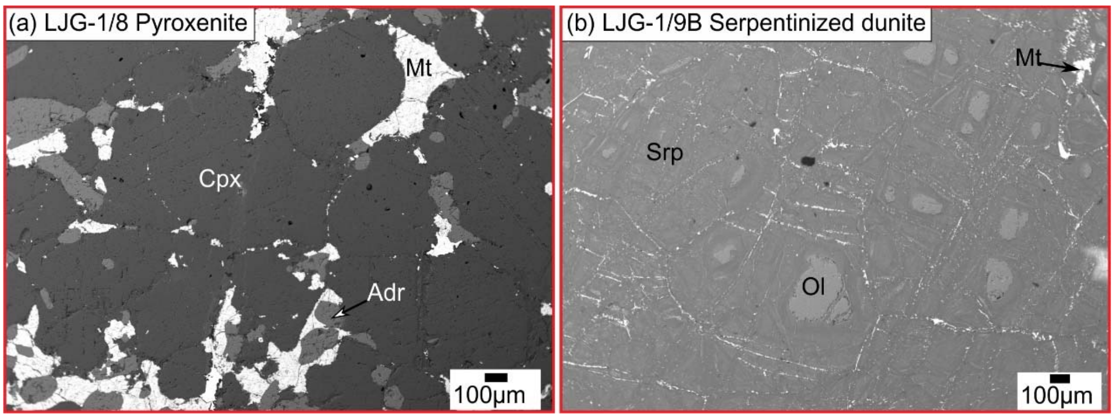
(a) LJG-1/8 Pyroxenite
Mt
Cpx
Adr
100μm
(b) LJG-1/9B Serpentinized dunite
Mt
Srp
Ol
100μm

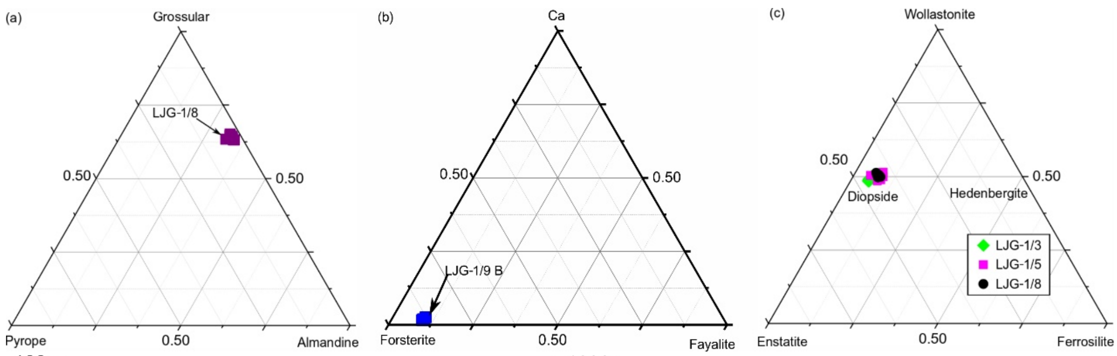
(a)
Grossular
LJG-1/8
0.50
0.50
Pyrope
0.50
Almandine
(b)
Ca
0.50
0.50
LJG-1/9 B
Forsterite
0.50
Fayalite
(c)
Wollastonite
0.50
0.50
Diopside
Hedenbergite
LJG-1/3
LJG-1/5
LJG-1/8
Enstatite
0.50
Ferrosilite

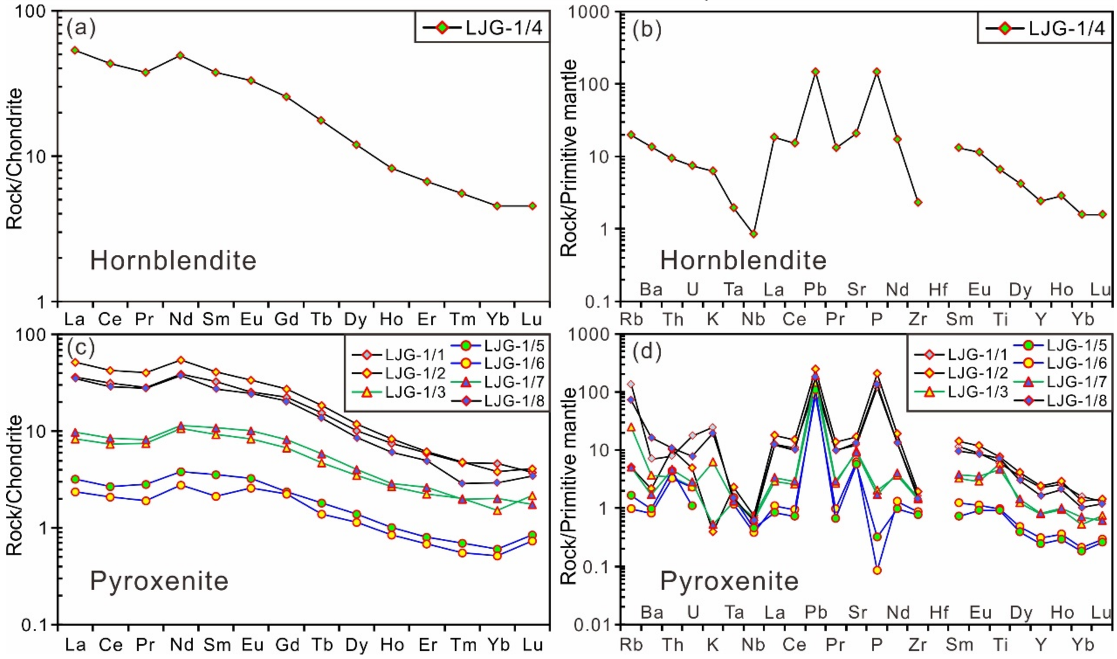
(a)
LJG-1/4
Rock/Chondrite
Hornblendite
La Ce Pr Nd Sm Eu Gd Tb Dy Ho Er Tm Yb Lu
(b)
LJG-1/4
Rock/Primitive mantle
Hornblendite
Rb Ba Th U K Ta Nb La Ce Pb Pr Sr P Nd Zr Hf Sm Eu Ti Dy Y Ho Yb Lu
(c)
LJG-1/1
LJG-1/2
LJG-1/3
LJG-1/5
LJG-1/6
LJG-1/7
LJG-1/8
Rock/Chondrite
Pyroxenite
La Ce Pr Nd Sm Eu Gd Tb Dy Ho Er Tm Yb Lu
(d)
LJG-1/1
LJG-1/2
LJG-1/3
LJG-1/5
LJG-1/6
LJG-1/7
LJG-1/8
Rock/Primitive mantle
Pyroxenite
Rb Ba Th U K Ta Nb La Ce Pb Pr Sr P Nd Zr Hf Sm Eu Ti Dy Y Ho Yb Lu

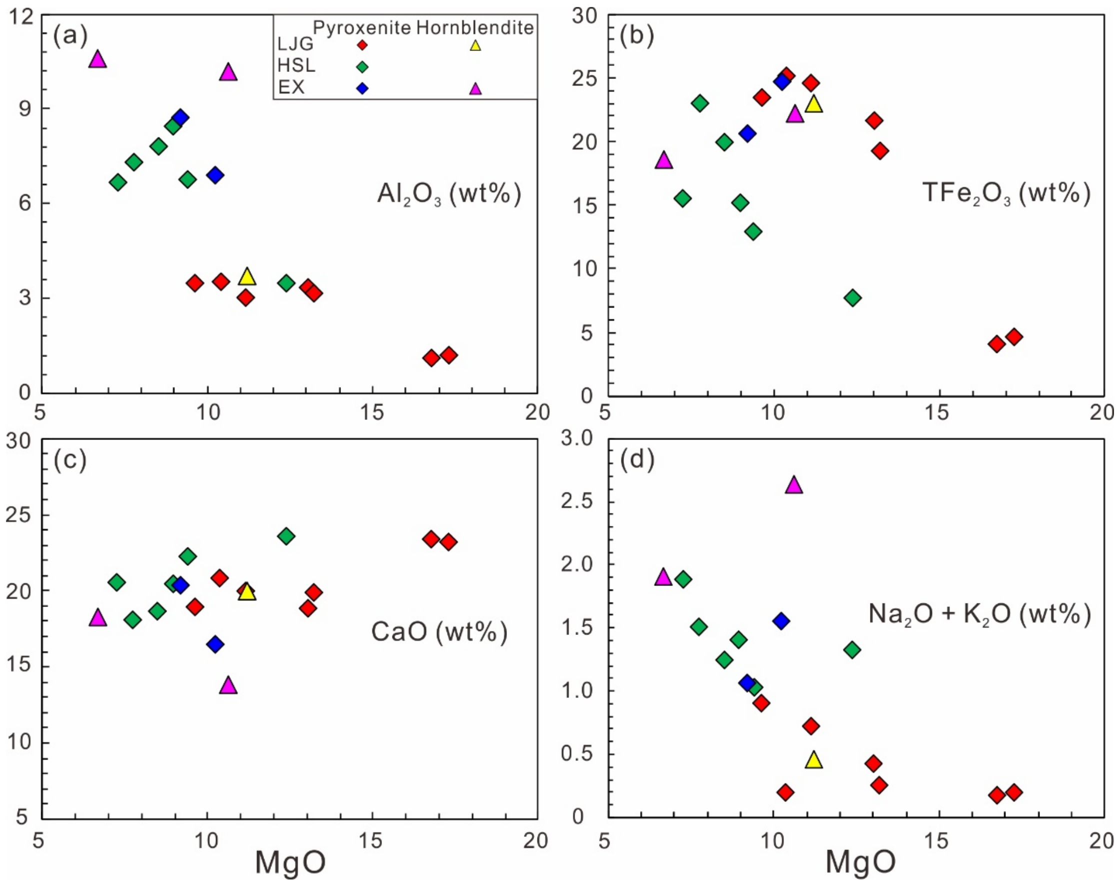
(a)
Pyroxenite Hornblendite
LJG
HSL
EX
Al2O3 (wt%)
(b)
TFe2O3 (wt%)
(c)
CaO (wt%)
(d)
Na2O + K2O (wt%)
MgO
MgO

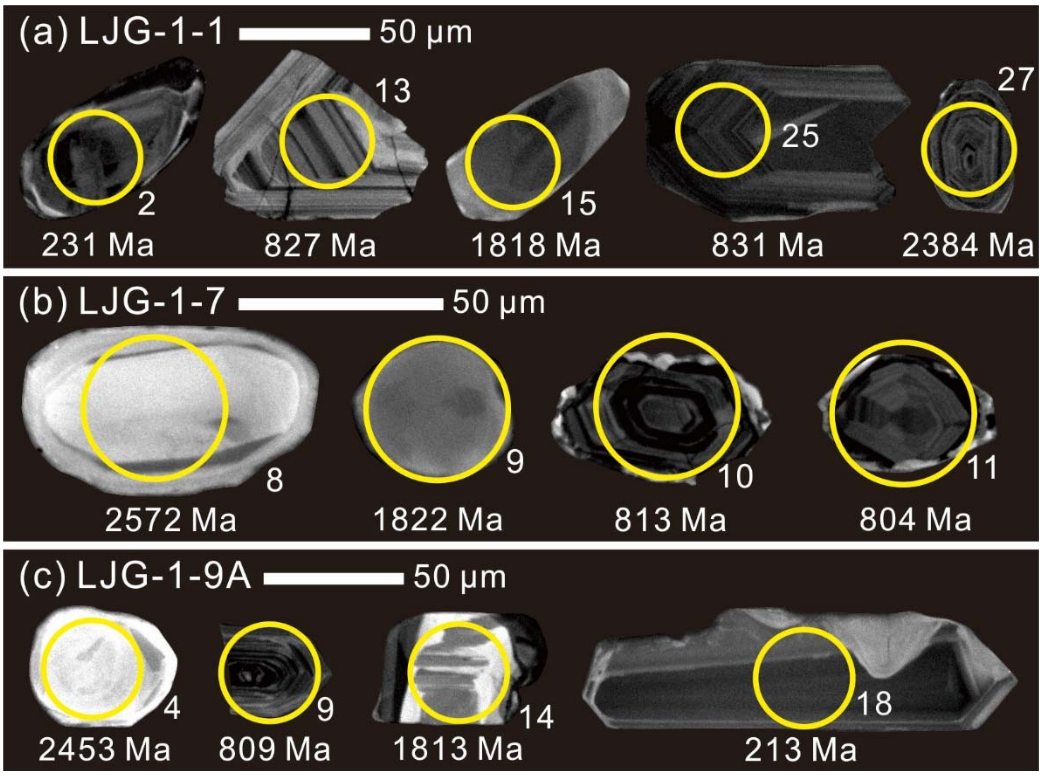
(a) LJG-1-1 50 μm
2
13
15
25
27
231 Ma
827 Ma
1818 Ma
831 Ma
2384 Ma
(b) LJG-1-7 50 μm
8
9
10
11
2572 Ma
1822 Ma
813 Ma
804 Ma
(c) LJG-1-9A 50 μm
4
9
14
18
2453 Ma
809 Ma
1813 Ma
213 Ma

1101

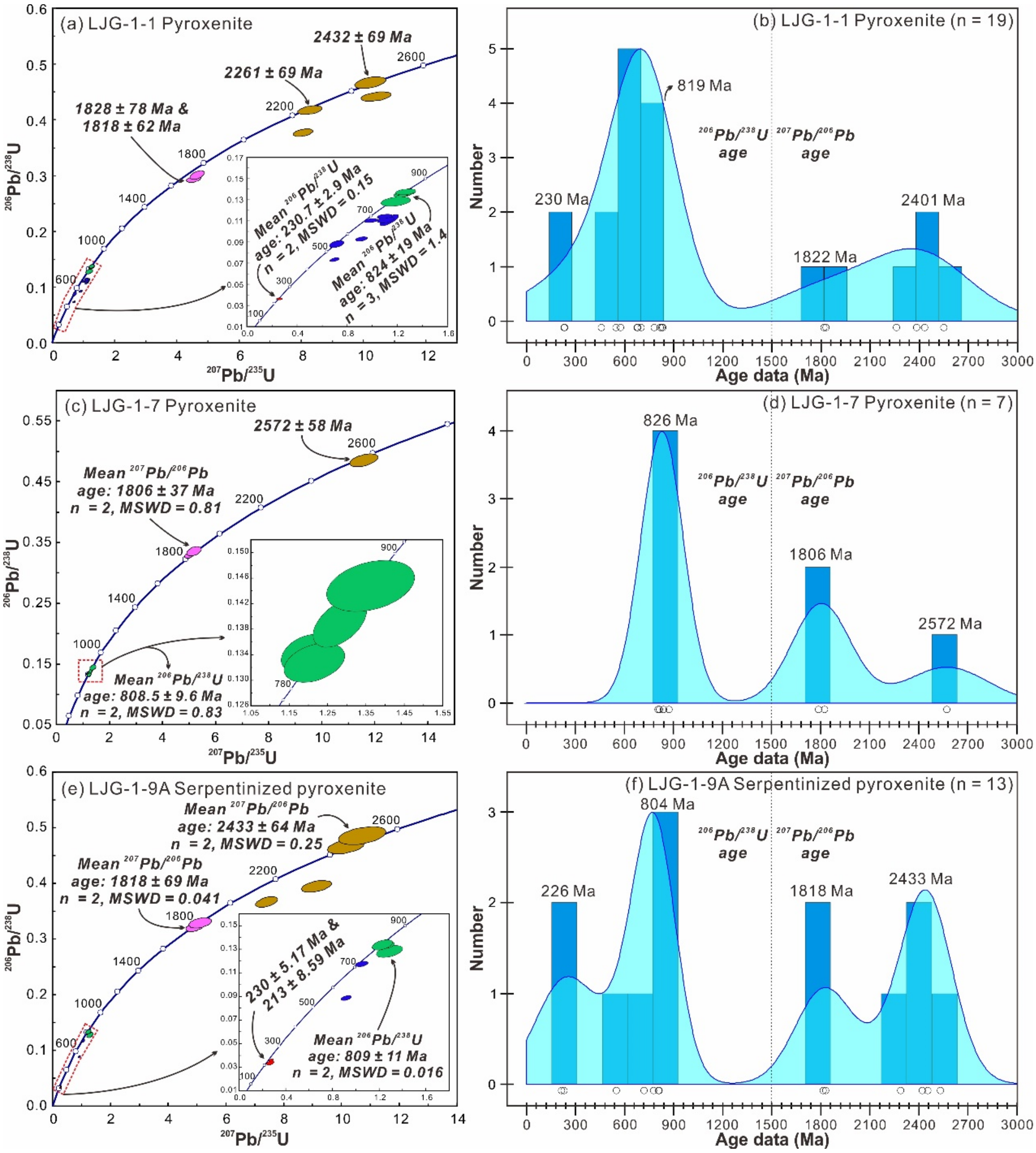
(a) LJG-1-1 Pyroxenite
2432 ± 69 Ma
2261 ± 69 Ma
1828 ± 78 Ma & 1818 ± 62 Ma
Mean 206Pb/238U age: 230.7 ± 2.9 Ma n = 2, MSWD = 0.15
Mean 206Pb/238U age: 824 ± 19 Ma n = 3, MSWD = 1.4
206Pb/238U
207Pb/235U
(b) LJG-1-1 Pyroxenite (n = 19)
819 Ma
230 Ma
2401 Ma
1822 Ma
206Pb/238U age
207Pb/206Pb age
Number
Age data (Ma)
(c) LJG-1-7 Pyroxenite
2572 ± 58 Ma
Mean 207Pb/206Pb age: 1806 ± 37 Ma n = 2, MSWD = 0.81
Mean 206Pb/238U age: 808.5 ± 9.6 Ma n = 2, MSWD = 0.83
(d) LJG-1-7 Pyroxenite (n = 7)
826 Ma
1806 Ma
2572 Ma
(e) LJG-1-9A Serpentinized pyroxenite
Mean 207Pb/206Pb age: 2433 ± 64 Ma n = 2, MSWD = 0.25
Mean 207Pb/206Pb age: 1818 ± 69 Ma n = 2, MSWD = 0.041
230 ± 5.17 Ma & 213 ± 8.59 Ma
Mean 206Pb/238U age: 809 ± 11 Ma n = 2, MSWD = 0.016
(f) LJG-1-9A Serpentinized pyroxenite (n = 13)
804 Ma
226 Ma
1818 Ma
2433 Ma

1102

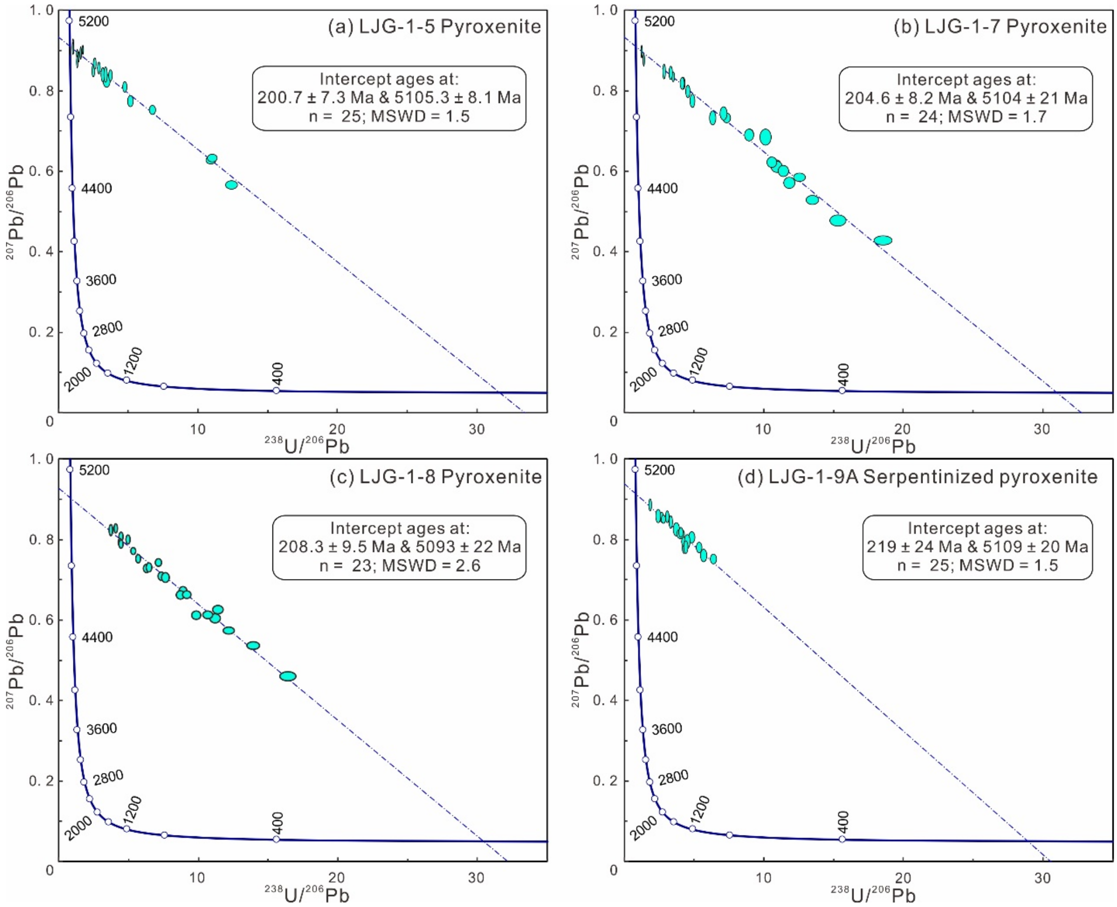
(a) LJG-1-5 Pyroxenite
Intercept ages at:
200.7 ± 7.3 Ma & 5105.3 ± 8.1 Ma
n = 25; MSWD = 1.5
(b) LJG-1-7 Pyroxenite
Intercept ages at:
204.6 ± 8.2 Ma & 5104 ± 21 Ma
n = 24; MSWD = 1.7
(c) LJG-1-8 Pyroxenite
Intercept ages at:
208.3 ± 9.5 Ma & 5093 ± 22 Ma
n = 23; MSWD = 2.6
(d) LJG-1-9A Serpentinized pyroxenite
Intercept ages at:
219 ± 24 Ma & 5109 ± 20 Ma
n = 25; MSWD = 1.5
207Pb/206Pb
238U/206Pb

1103

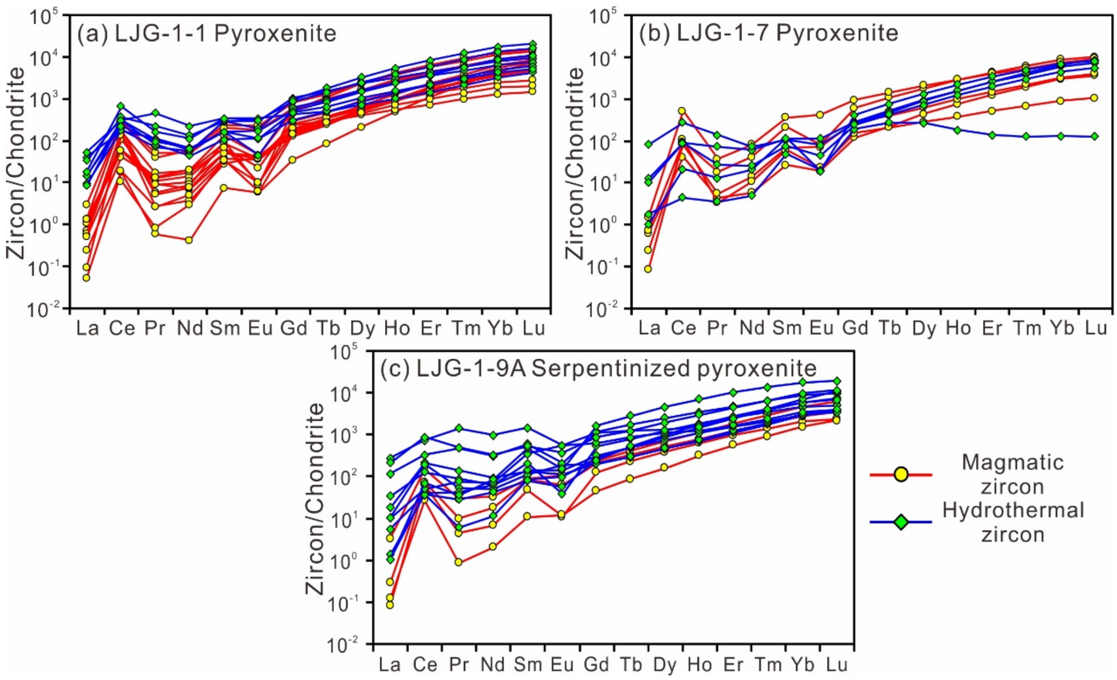
(a) LJG-1-1 Pyroxenite
(b) LJG-1-7 Pyroxenite
(c) LJG-1-9A Serpentinized pyroxenite
Zircon/Chondrite
La Ce Pr Nd Sm Eu Gd Tb Dy Ho Er Tm Yb Lu
Magmatic zircon
Hydrothermal zircon

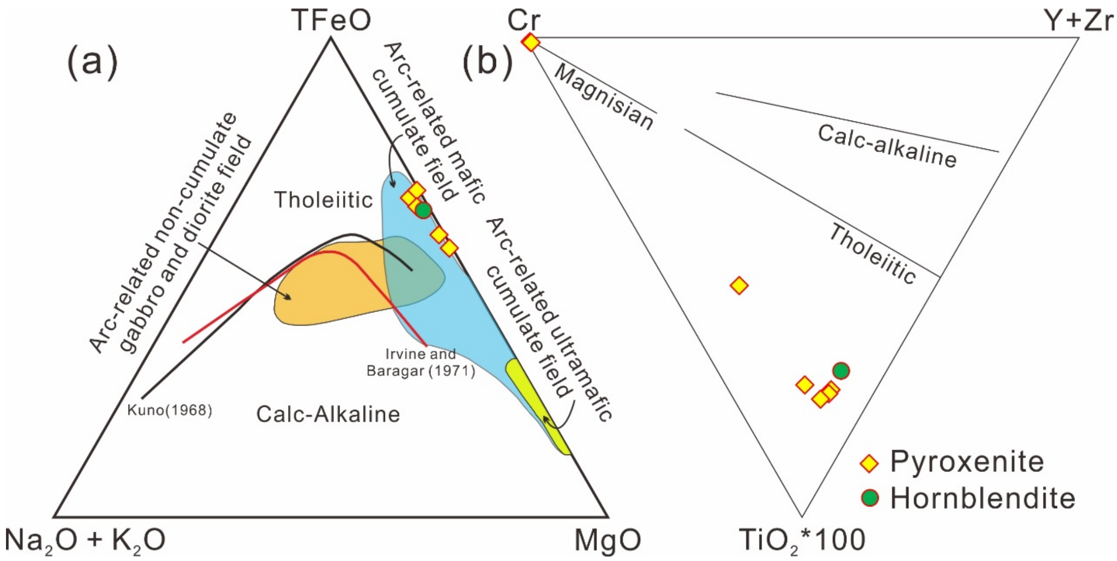
(a)
TFeO
Arc-related non-cumulate gabbro and diorite field
Arc-related mafic cumulate field
Tholeiitic
Arc-related ultramafic cumulate field
Irvine and Baragar (1971)
Kuno(1968)
Calc-Alkaline
$Na_2O + K_2O$
MgO
(b)
Cr
Y+Zr
Magnisian
Calc-alkaline
Tholeiitic
Pyroxenite
Hornblendite
TiO_2*100

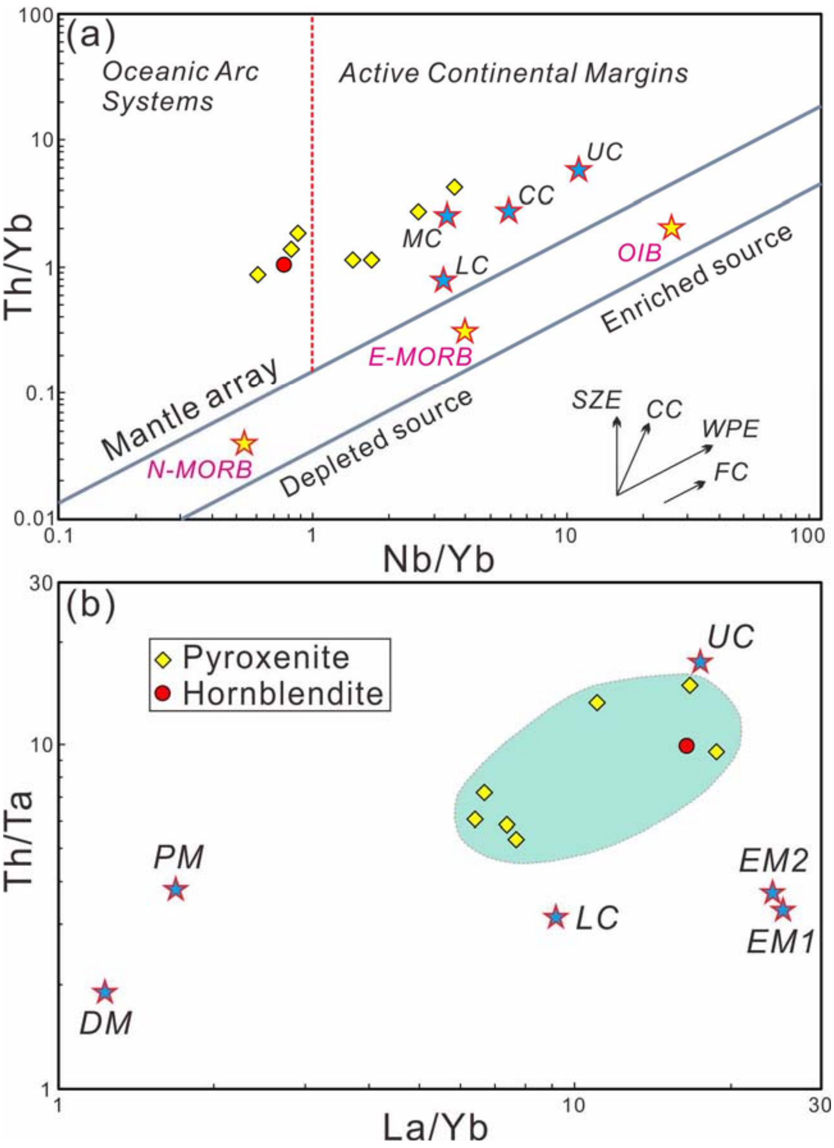
(a)
Oceanic Arc Systems
Active Continental Margins
UC
CC
MC
LC
OIB
Enriched source
Mantle array
E-MORB
N-MORB
Depleted source
SZE
CC
WPE
FC
Th/Yb
Nb/Yb
(b)
Pyroxenite
Hornblendite
UC
PM
LC
EM2
EM1
DM
Th/Ta
La/Yb

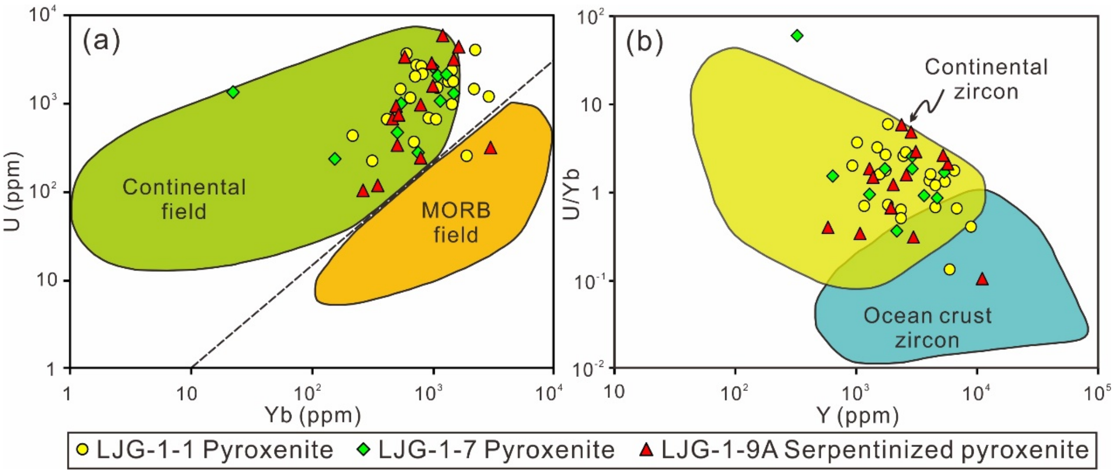

(a)
(b)
Continental field
MORB field
Continental zircon
Ocean crust zircon
U (ppm)
Yb (ppm)
U/Yb
Y (ppm)
LJG-1-1 Pyroxenite
LJG-1-7 Pyroxenite
LJG-1-9A Serpentinized pyroxenite

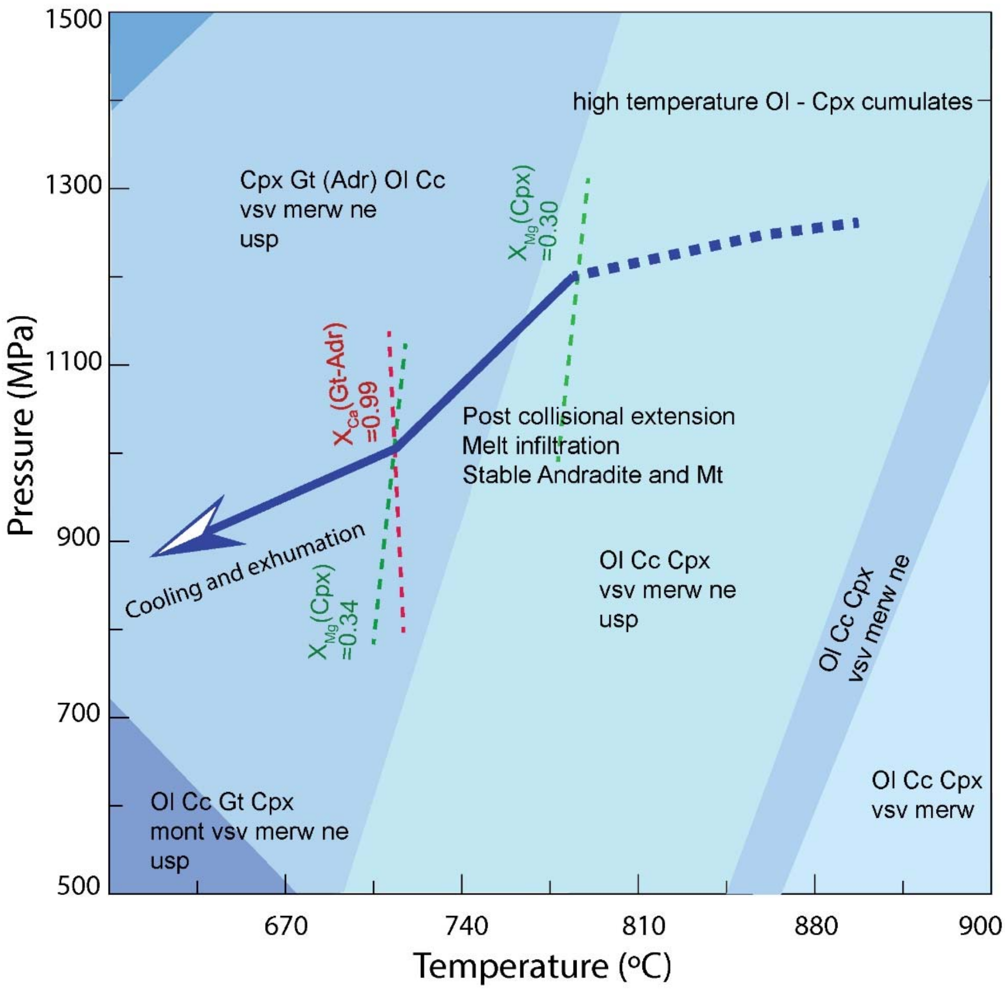

high temperature Ol - Cpx cumulates
Cpx Gt (Adr) Ol Cc
vsv merw ne
usp
X_{Mg}(Cpx) =0.30
X_{Ca}(Gt-Adr) =0.99
Post collisional extension
Melt infiltration
Stable Andradite and Mt
Cooling and exhumation
X_{Mg}(Cpx) =0.34
Ol Cc Cpx
vsv merw ne
usp
Ol Cc Cpx
vsv merw ne
Ol Cc Gt Cpx
mont vsv merw ne
usp
Ol Cc Cpx
vsv merw
Pressure (MPa)
Temperature (°C)

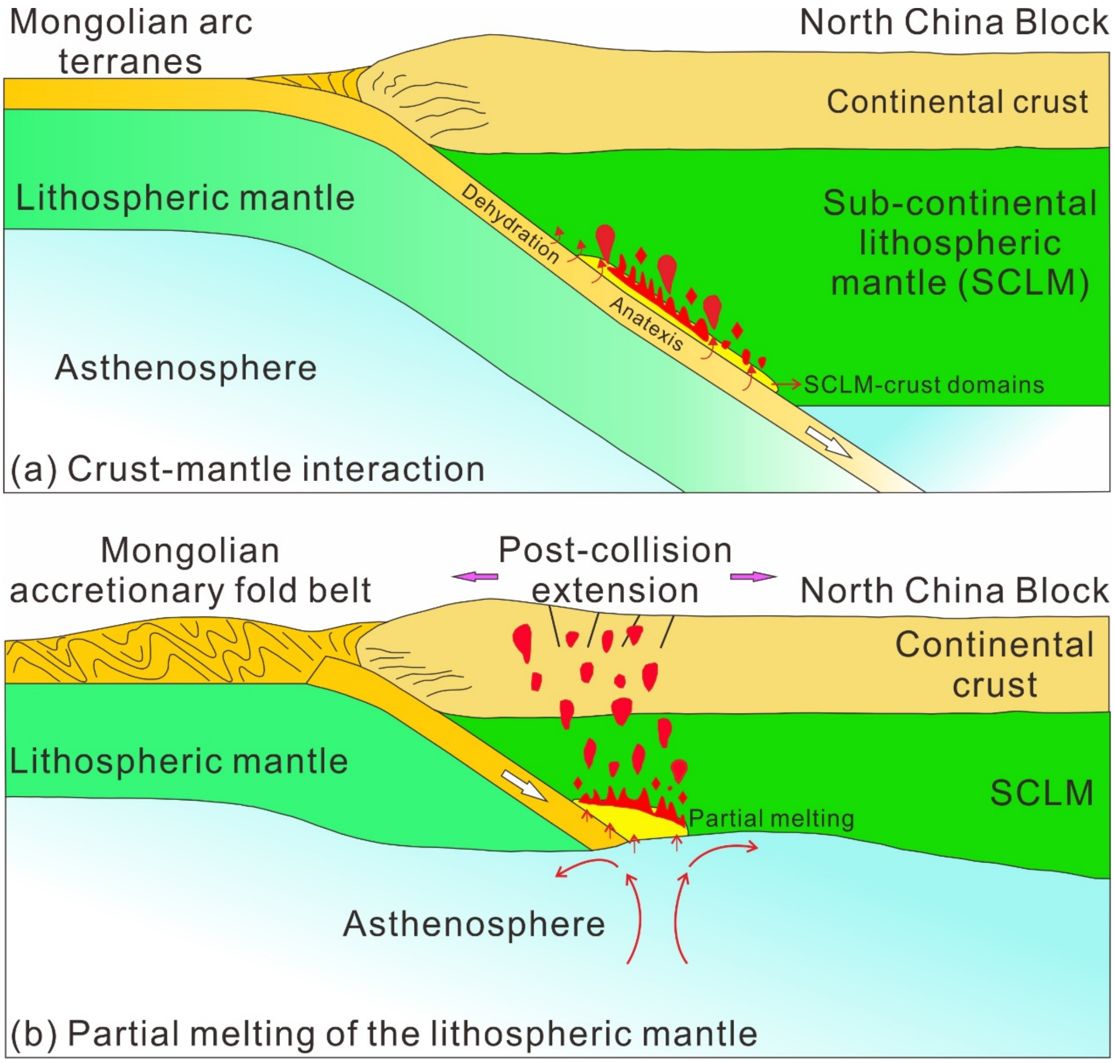
Mongolian arc terranes
North China Block
Continental crust
Lithospheric mantle
Sub-continental lithospheric mantle (SCLM)
Dehydration
Anatexis
Asthenosphere
SCLM-crust domains
(a) Crust-mantle interaction
Mongolian accretionary fold belt
Post-collision extension
North China Block
Continental crust
Lithospheric mantle
SCLM
Partial melting
Asthenosphere
(b) Partial melting of the lithospheric mantle